

A hybridized discontinuous Galerkin framework for high-order particle–mesh operator splitting of the incompressible Navier–Stokes equations

Maljaars, Jakob M.; Labeur, Robert Jan; Möller, Matthias

DOI

[10.1016/j.jcp.2017.12.036](https://doi.org/10.1016/j.jcp.2017.12.036)

Publication date

2018

Document Version

Accepted author manuscript

Published in

Journal of Computational Physics

Citation (APA)

Maljaars, J. M., Labeur, R. J., & Möller, M. (2018). A hybridized discontinuous Galerkin framework for high-order particle–mesh operator splitting of the incompressible Navier–Stokes equations. *Journal of Computational Physics*, 358, 150-172. <https://doi.org/10.1016/j.jcp.2017.12.036>

Important note

To cite this publication, please use the final published version (if applicable). Please check the document version above.

Copyright

Other than for strictly personal use, it is not permitted to download, forward or distribute the text or part of it, without the consent of the author(s) and/or copyright holder(s), unless the work is under an open content license such as Creative Commons.

Takedown policy

Please contact us and provide details if you believe this document breaches copyrights. We will remove access to the work immediately and investigate your claim.

A hybridized discontinuous Galerkin framework for high-order particle-mesh operator splitting of the incompressible Navier-Stokes equations

Jakob M. Maljaars^{a,*}, Robert Jan Labeur^a, Matthias Möller^b

^a*Environmental Fluid Mechanics, Faculty of Civil Engineering and Geosciences, Delft University of Technology, P.O. Box 5048, Stevinweg 1, 2600 GA Delft, The Netherlands*

^b*Department of Applied Mathematics, Delft University of Technology, Mekelweg 4, 2628 CD Delft, The Netherlands*

Abstract

A generic particle-mesh method using a hybridized discontinuous Galerkin (HDG) framework is presented and validated for the solution of the incompressible Navier-Stokes equations. Building upon particle-in-cell concepts, the method is formulated in terms of an operator splitting technique in which Lagrangian particles are used to discretize an advection operator, and an Eulerian mesh-based HDG method is employed for the constitutive modeling to account for the inter-particle interactions. Key to the method is the variational framework provided by the HDG method. This allows to formulate the projections between the Lagrangian particle space and the Eulerian finite element space in terms of local (i.e. cellwise) ℓ^2 -projections efficiently. Furthermore, exploiting the HDG framework for solving the constitutive equations results in velocity fields which excellently approach the incompressibility constraint in a local sense. By advecting the particles through these velocity fields, the particle distribution remains uniform over time, obviating the need for additional quality control. The presented methodology allows for a straightforward extension to arbitrary-order spatial accuracy on general meshes. A range of numerical examples shows that optimal convergence rates are obtained in space and, given the particular time stepping strategy, second-order accuracy is obtained in time. The model capabilities are further demonstrated by presenting results for the flow over a backward facing step and for the flow around a cylinder.

Keywords: incompressible Navier-Stokes equations, Lagrangian-Eulerian, hybridized discontinuous Galerkin, finite elements, particle-in-cell, material point method

1. Introduction

Over the past decades, a wealth of numerical methods has been developed in the Computational Fluid Dynamics (CFD) community. These methods can roughly be categorized in two different classes. On the one

*Corresponding author

Email addresses: j.m.maljaars@tudelft.nl (Jakob M. Maljaars), r.j.labeur@tudelft.nl (Robert Jan Labeur), m.moller@tudelft.nl (Matthias Möller)

side, purely Eulerian methods solve the governing equations on a static mesh topology using the finite difference (FD), finite volume (FV) or finite element (FEM) approach. On the other side, purely Lagrangian methods, such as smoothed particle hydrodynamics (SPH) and the moving particle semi-implicit (MPS) method, use a set of moving particles to track material properties.

In an attempt to reconcile both approaches, hybrid particle-mesh methods make a combined use of Lagrangian particles and an Eulerian background mesh. A hybrid particle-mesh method can be interpreted as an operator splitting technique in which the problem kinematics are solved in a Lagrangian framework, by using moving particles to discretize an advection operator, while a fixed Eulerian mesh is used for the constitutive modeling to account for the inter-particle interactions. This approach avoids the expensive construction of particle neighbor lists as required in fully Lagrangian, particle-based methods. Furthermore, a wealth of existing solvers can be used to efficiently solve the constitutive equations at the Eulerian mesh.

Particle-mesh methods trace back to the 1950s with the development of the particle-in-cell method (PIC) [1]. Ever since, many variations to the original approach have been proposed. The fluid implicit particle (FLIP) method was introduced by Brackbill and Ruppel [2] in order to reduce the numerical diffusion of the original PIC formulation. The FLIP method became especially popular in the computer graphics industry (see e.g. [3]). Moreover, in recent work the method has also been applied in an engineering context for simulating free-surface flows [4, 5, 6]. An extension of the FLIP method to history-dependent materials was made by Sulsky and coworkers [7]. Their method is currently known as the material point method (MPM) and is especially popular for simulating large deformation problems in solid mechanics. Recently, various attempts have been made to use MPM for the simulation of incompressible fluid flows [8, 9]. Despite the attractive features of particle-mesh methods and the wide variety of implementations found in literature, various difficulties remain persistent to these methods.

A first issue is the coupling between the particles and the mesh, which is responsible for the transfer of information from the particles to the mesh and *vice versa*. For an overview of various coupling strategies on regular Cartesian meshes, the reader is referred to [10]. A common approach adopted in the MPM is to consider the particles as moving quadrature points and setting their weight equal to the material point mass. This approach, however, may compromise accuracy due to grid-crossing errors, which occur when particles experience an abrupt change in acceleration when moving from one grid cell into the other. Moreover, non-Gaussian quadrature of this type yields non-optimal accuracy. Attempts have been made to mitigate these problems by using basis functions being at least C^1 -continuous [11, 12], or by using a blend between optimal quadrature and quadrature based on moving material points [8]. The implications of the latter approach, in terms of accuracy and physical consistency, remain unknown however. An alternative strategy, which allows for high-order spatial accuracy, is to first reconstruct continuous fields at the Eulerian mesh from the scattered particle data and apply standard quadrature rules in a second step. The reconstruction of the continuous fields is done using, e.g., spline reconstruction techniques [12], which leads to global systems for

the projection steps, or a moving least-squares (MLS) projection [13, 14], which requires the choice of an appropriate particle weighting function. In general, this renders the influence of a particle non-local to its hosting cell, which increases algorithmic complexity and computational costs.

A second issue, related to particle-mesh methods for (incompressible) flow problems, is the degradation of an initially uniform particle distribution into a non-uniform distribution containing voids and clusters of particles. In fact, this artifact is shared with fully Lagrangian, particle-based methods such as SPH (see e.g. [15, 16]). Pope [17] identifies inaccuracies in the divergence of the advective velocity field to be among the main reasons for the degradation of the particle distribution. Based on this observation, various authors have proposed velocity field reconstruction techniques in order to maintain uniform particle distributions in the incompressible limit [18, 19, 20]. In these references, the reconstructed velocity fields are required to be locally (i.e. cellwise or even pointwise) divergence-free in order to maintain a uniform particle distribution, while also an accurate particle advection scheme must be used. Other authors pursue a more heuristic particle distribution quality control by either introducing weak spring forces between particles [4, 15, 21], or by using particle re seeding [13] or particle splitting [16] techniques.

The aim of this paper is the formulation of a generic particle-mesh method for the solution of the incompressible Navier-Stokes equations on arbitrary meshes, using a hybridized discontinuous Galerkin (HDG) framework. The presented approach allows for an accurate and efficient transfer of information between the particles and the mesh, and is able to maintain a uniform particle distribution over time. Key to the former is the reconstruction of piecewise-continuous fields at the Eulerian mesh from the scattered particle data using ℓ^2 -projections. These projections can be interpreted as a specialized MLS-reconstruction and remain local (i.e. cellwise) since the scattered particle data is projected onto the piecewise-continuous HDG basis functions. The reconstructed fields serve as an input to the HDG method developed by Labeur and Wells [22] which is used to solve the constitutive equations at the background mesh. Owing to the excellent local mass conservation properties of this method, the local divergence errors in the resulting velocity fields are sufficiently small to maintain a uniform particle distribution when advecting the particles through these velocity fields. This obviates the need for additional measures such as velocity field reconstruction techniques or heuristic particle shifting algorithms, as demonstrated by various numerical examples.

The remainder of this paper is structured as follows. In Section 2, the problem of interest is formulated and the corresponding operator splitting technique is introduced, leading to a decomposition of the overall problem into two subproblems: an advection problem and an incompressible Stokes problem. Section 3 details a generic approach for these respective subproblems, and the coupling between them by means of two auxiliary projection steps. Section 4 presents a fully discrete formulation for the various steps involved and further motivates the choice for an HDG approach in combination with ℓ^2 -projections between the particles and the mesh by highlighting various attractive features of the resulting scheme. Section 5 presents convergence and error analyses by comparing simulated results with analytical solutions. Special attention

is paid to the quality of the particle distribution and to the conservation of discrete momentum. In addition,
75 the results for two benchmark tests are presented in this section. Conclusions and an outlook for future
research are presented in Section 6.

2. Governing equations and definitions

2.1. Governing equations

Consider a domain $\Omega \subset \mathbb{R}^d$, with $d = 2, 3$ the number of spatial dimensions, having a Lipschitz continuous
80 boundary $\Gamma = \partial\Omega$ which is partitioned into Dirichlet - and Neumann boundaries Γ_D and Γ_N , respectively,
such that $\Gamma_D \cup \Gamma_N = \partial\Omega$ and $\Gamma_D \cap \Gamma_N = \emptyset$. The unit vector normal to Γ pointing outward is denoted
with \mathbf{n} . The time interval of interest is $I = [t^0, t^N]$, where t^0 and t^N are the start - and end time of the
simulation, respectively.

On the space-time domain $\Omega \times I$ the incompressible Navier-Stokes equations are stated as follows: given
85 the kinematic viscosity ν , the forcing term $\mathbf{f} : \Omega \times I \rightarrow \mathbb{R}^d$, the boundary conditions $\mathbf{g} : \Gamma_D \times I \rightarrow \mathbb{R}^d$ and
 $\mathbf{h} : \Gamma_N \times I \rightarrow \mathbb{R}^d$, and a solenoidal initial condition $\mathbf{u}_0 : \Omega \rightarrow \mathbb{R}^d$, find the velocity field $\mathbf{u} : \Omega \times I \rightarrow \mathbb{R}^d$ and
the pressure field $p : \Omega \times I \rightarrow \mathbb{R}$ such that

$$\frac{\partial \mathbf{u}}{\partial t} + \mathbf{u} \cdot \nabla \mathbf{u} + \nabla \cdot \boldsymbol{\sigma} = \mathbf{f} \quad \text{in } \Omega \times I, \quad (1)$$

$$\nabla \cdot \mathbf{u} = 0 \quad \text{in } \Omega \times I, \quad (2)$$

90
$$\boldsymbol{\sigma} = p\mathbf{I} - 2\nu\nabla^s \mathbf{u} \quad \text{in } \Omega \times I, \quad (3)$$

$$\mathbf{u} = \mathbf{g} \quad \text{on } \Gamma_D \times I, \quad (4)$$

$$(\gamma \mathbf{u} \otimes \mathbf{u} + \boldsymbol{\sigma}) \mathbf{n} = \mathbf{h} \quad \text{on } \Gamma_N \times I, \quad (5)$$

$$\mathbf{u}(\mathbf{x}, 0) = \mathbf{u}_0(\mathbf{x}) \quad \text{in } \Omega, \quad (6)$$

95 where $\boldsymbol{\sigma}$ is the diffusive momentum flux tensor, \mathbf{I} is the identity tensor, and $\nabla^s \mathbf{u} = \frac{1}{2}\nabla(\mathbf{u}) + \frac{1}{2}\nabla(\mathbf{u})^\top$ is
the symmetric velocity-gradient tensor. The factor γ is equal to one on inflow parts of Γ_N (that is, where
 $\mathbf{u} \cdot \mathbf{n} < 0$), imposing in this way the total momentum flux. On the outflow parts of Γ_N (where $\mathbf{u} \cdot \mathbf{n} \geq 0$),
the factor γ equals zero which prescribes the diffusive part of the momentum flux only.

2.2. Operator splitting

100 An approach often used for solving the incompressible Navier-Stokes equations is to decompose the
problem into a sequence of simpler subproblems by using operator splitting. Such a splitting procedure
may either decouple the advection-diffusion problem from the incompressibility constraint (see e.g. the
splitting method proposed by Chorin and Temam [23, 24]), or it may decouple the advection problem from
the incompressible Stokes problem (see e.g. the method proposed by Glowinski [25]). Similarly to the latter

105 approach, we split the governing equations (1-6) into an advection problem and an incompressible Stokes problem. For illustrative purposes we present a particular splitting procedure below, containing the essential components.

To this end, the time interval of interest I is partitioned using a sequence of $N + 1$ discrete time levels $\{t^0, t^1, \dots, t^{N-1}, t^N\}$ which for $n = 0, N - 1$ defines the subintervals $I_n = [t^n, t^{n+1}]$ such that $\bigcup_n I_n = I$.

110 Our operator splitting procedure involves a velocity field \mathbf{v} solving an advection problem:

$$\frac{\partial \mathbf{v}}{\partial t} + \mathbf{v} \cdot \nabla \mathbf{v} = \mathbf{0} \quad \text{in } \Omega \times I_n, \quad (7)$$

$$\mathbf{v} = \mathbf{g} \quad \text{on } \Gamma_D^- \times I_n, \quad (8)$$

$$(\gamma \mathbf{v} \otimes \mathbf{v}) \mathbf{n} = \mathbf{h}_a \quad \text{on } \Gamma_N \times I_n, \quad (9)$$

$$115 \quad \mathbf{v}(\mathbf{x}, t^n) = \mathcal{P}_L(\mathbf{u}(\mathbf{x}, t^n)) \quad \text{in } \Omega, \quad (10)$$

and a velocity field \mathbf{u} solving a subsequent Stokes problem:

$$\frac{\partial \mathbf{u}}{\partial t} + \nabla \cdot \boldsymbol{\sigma} = \mathbf{f} \quad \text{in } \Omega \times I_n, \quad (11)$$

$$\nabla \cdot \mathbf{u} = 0 \quad \text{in } \Omega \times I_n, \quad (12)$$

$$\boldsymbol{\sigma} = p\mathbf{I} - 2\nu\nabla^s \mathbf{u} \quad \text{in } \Omega \times I_n, \quad (13)$$

$$120 \quad \mathbf{u} = \mathbf{g} \quad \text{on } \Gamma_D \times I_n, \quad (14)$$

$$\boldsymbol{\sigma} \mathbf{n} = \mathbf{h}_d \quad \text{on } \Gamma_N \times I_n, \quad (15)$$

$$\mathbf{u}(\mathbf{x}, t^n) = \mathcal{P}_E(\mathbf{v}(\mathbf{x}, t^{n+1})) \quad \text{in } \Omega. \quad (16)$$

In Eq. (8), Γ_D^- denotes the inflow part of the Dirichlet boundary, and \mathbf{h}_a and \mathbf{h}_d denote the advective and
 125 diffusive momentum flux on Γ_N , respectively, such that $\mathbf{h} = \mathbf{h}_a + \mathbf{h}_d$, with this splitting being based on physical arguments. Furthermore, \mathcal{P}_L and \mathcal{P}_E denote projection operators to provide the conditions at t^n for advancing the solution to t^{n+1} for the advection problem and the Stokes problem, respectively. It is required that $\mathbf{v}(\mathbf{x}, t^0) = \mathcal{P}_L(\mathbf{u}(\mathbf{x}, t^0)) = \mathbf{u}_0(\mathbf{x})$ in order to satisfy Eq. (6).

The proposed method employs a Lagrangian (particle-based) strategy to solve the advection problem
 130 (Eqs. (7-10)), and an Eulerian (mesh-based) method to solve the unsteady Stokes problem (Eqs. (11-16)), where the projection operators \mathcal{P}_L and \mathcal{P}_E essentially couple the velocity field \mathbf{v} associated with the Lagrangian particles and the velocity field \mathbf{u} associated with the Eulerian mesh.

Subsequent use of Eqs. (7-16) for $n = 0, 1, \dots, N - 1$ leads to a recurrent time marching scheme in I . Many variations to this splitting procedure can be constructed by rearranging the different components. For an
 135 overview of different operator splitting techniques a reference is made to e.g. [25].

2.3. Definitions

Throughout the paper, the following definitions are adopted in order to discretize the various fields. The fixed Eulerian mesh is the triangulation $\mathcal{T} := \{K\}$ of the domain Ω into open and non-overlapping cells K . A measure of the cell size is denoted by h_K and the outward pointing unit normal vector on the boundary ∂K of each cell is denoted by \mathbf{n} . The closure of a cell is denoted by $\bar{K} = K \cup \partial K$. Adjacent cells K_i and K_j share a common facet $F = \bar{K}_i \cap \bar{K}_j$, the union of all facets (including the exterior boundary facets $F = \bar{K} \cap \partial\Omega$) is denoted by $\Gamma^0 = \bigcup F$, and $\mathcal{F} := \{F\}$ is the set of all facets.

The following vector finite element function spaces are defined:

$$W_h := \left\{ \mathbf{w}_h \in [L^2(\Omega)]^d, \mathbf{w}_h|_K \in [P_k(K)]^d \forall K \in \mathcal{T} \right\}, \quad (17)$$

$$\bar{W}_{h,g} := \left\{ \bar{\mathbf{w}}_h \in [H^{1/2}(\Gamma^0)]^d, \bar{\mathbf{w}}_h|_F \in [P_k(F)]^d \forall F \in \mathcal{F}, \bar{\mathbf{w}}_h = \mathbf{g} \text{ on } \Gamma_D \right\}, \quad (18)$$

in which $[H^{1/2}(\Gamma^0)]^d$ is the trace space of $[H^1(\Omega)]^d$ on Γ^0 , and where $P_k(K)$ and $P_k(F)$ denote the spaces spanned by Lagrange polynomials on K and F , respectively, with $k \geq 1$ being the polynomial order. It is noted that the space W_h contains vector valued functions which are discontinuous across cell boundaries, whereas the continuous functions in $\bar{W}_{h,g}$ are only defined on cell facets and satisfy the inhomogeneous Dirichlet boundary values on Γ_D . Furthermore, $\bar{W}_{h,0}$ denotes the space associated with $\bar{W}_{h,g}$ which satisfies the homogeneous Dirichlet boundary condition on Γ_D .

Element and facet related scalar function spaces are defined as, respectively

$$Q_h := \left\{ q_h \in L^2(\Omega), q_h|_K \in P_m(K) \forall K \in \mathcal{T} \right\}, \quad (19)$$

$$\bar{Q}_h := \left\{ \bar{q}_h \in H^{1/2}(\Gamma^0), \bar{q}_h|_F \in P_m(F) \forall F \in \mathcal{F} \right\}, \quad (20)$$

where $H^{1/2}(\Gamma^0)$ is the trace space of $H^1(\Omega)$ on Γ^0 , and $m \geq 1$ is the polynomial order.

The Lagrangian particle configuration in the domain Ω at a fixed time instant t is denoted by

$$\mathcal{X}_t := \{\mathbf{x}_p(t) \in \Omega\}_{p=1}^{N_p}, \quad (21)$$

in which \mathbf{x}_p denotes the spatial coordinates of particle p and N_p is the number of particles.

A Lagrangian field on the particles is defined as

$$\mathcal{V}_t := \{\mathbf{v}_p(t) \in \mathbb{R}^d, \mathbf{x}_p(t) \in \mathcal{X}_t \forall p\}, \quad (22)$$

where \mathbf{v}_p is a vector quantity associated with the particle. In the sequel \mathbf{v}_p will be used to denote the specific momentum carried by a particle.

For notational convenience, the index set of particles is defined as

$$\mathcal{S}_t := \{p \in \mathbb{N}, \mathbf{x}_p(t) \in \mathcal{X}_t\}, \quad (23)$$

and finally, the index set of particles hosted by cell K at a fixed time instant t is given by

$$\mathcal{S}_t^K := \{p \in \mathbb{N}, \mathbf{x}_p(t) \in \bar{K}\}. \quad (24)$$

3. Semi-discrete components of the hybrid particle-mesh operator splitting

Key to the presented particle-mesh method is the splitting of the semi-discrete problem into a Lagrangian step and an Eulerian step. As argued above, this strategy requires a transfer of information from the Eulerian mesh to the Lagrangian particles and *vice versa* by means of two projection steps (i.e. Eqs. (10) and (16), respectively). These auxiliary projection steps involve the reconstruction of a velocity field at the mesh from the scattered particle data, and the update of the specific momentum carried by the particles, given the velocity field at the mesh.

In summary, the proposed particle-mesh method has the following principal components:

1. *Lagrangian discretization of the advection problem*; in order to solve Eqs. (7-9).
2. *Eulerian discretization of the (unsteady) Stokes problem*; in order to solve Eqs. (11-15).
3. *Particle-mesh projection*; reconstruct a velocity field at the Eulerian mesh from the scattered particles in order to advance the Stokes problem in time (Eq. (16)).
4. *Mesh-particle projection*; given the solution at the Eulerian mesh, update the specific momentum of the particles in order to advance the advection problem in time (Eq. (10)).

This section presents a generic semi-discrete formulation for the steps listed above, using an HDG framework. A particular, fully-discrete solution procedure is presented in Section 4, and the algorithmic aspects of the developed solution strategy are briefly evaluated in Section 4.5.

3.1. Lagrangian discretization of advection problem

In a Lagrangian, particle-based, frame of reference, the nonlinear advection problem (Eqs. (7-10)) can be decomposed into two ordinary differential equations for the particle velocity and the particle position, given by, respectively

$$\dot{\mathbf{v}}_p(t) = \mathbf{0} \quad \forall p \in \mathcal{S}_t, \quad (25)$$

$$\dot{\mathbf{x}}_p(t) = \tilde{\mathbf{v}}(\mathbf{x}_p(t), t) \quad \forall p \in \mathcal{S}_t. \quad (26)$$

In these equations, $\dot{\mathbf{v}}_p$ and $\dot{\mathbf{x}}_p$ denote the time derivative of the velocity and the position of particle p at time instant t , respectively. Furthermore, $\tilde{\mathbf{v}}$ denotes an advective velocity field to be specified below, but with the minimal requirement of satisfying the boundary constraints Eqs. (8-9).

3.2. Eulerian discretization of the Stokes problem

Of the various HDG schemes for the (Navier-)Stokes equations presented in literature (see, e.g., [22, 26, 27]), this study employs the HDG method developed by Labour and Wells [22] for the spatial discretization of the unsteady Stokes problem (Eqs. (11-15)). A brief summary of this method is provided below. For an in-depth description and analysis of the method, reference is made to the aforementioned paper as well as

[28].

Splitting the equations into local (i.e. cellwise) and global balances is central to the HDG method: the local equations represent cellwise balances and the global equations are formulated by enforcing weakly the continuity of the mass and momentum fluxes across cell facets. The local balances on a cell are linked to the local balances on neighboring cells only via globally defined facet functions, thus circumventing a direct interaction between neighboring cells [22].

A Galerkin approximation of the local mass balance (i.e. the incompressibility constraint, given by Eq. (12)), requires the local velocity field $\mathbf{u}_h \in W_h$ to satisfy

$$\sum_K \int_K \mathbf{u}_h \cdot \nabla q_h d\Omega - \sum_K \int_{\partial K} \hat{\mathbf{u}}_h \cdot \mathbf{n} q_h d\Gamma = 0 \quad \forall q_h \in Q_h, \quad (27)$$

where the numerical mass flux $\hat{\mathbf{u}}_h$ on ∂K is defined as

$$\hat{\mathbf{u}}_h = \mathbf{u}_h - \frac{\beta h_K}{\nu + 1} (\bar{p}_h - p_h) \mathbf{n}, \quad (28)$$

in which $p_h \in Q_h$ the local pressure field, $\bar{p}_h \in \bar{Q}_h$ is the global (facet) pressure field, ν is the kinematic viscosity and β is a stability parameter [22]. Note that the numerical mass flux can take on different values on opposite sides of a facet. Furthermore, the pressure-stabilizing term in Eq. (28) only involves the difference between the globally defined pressure on the facets \bar{p}_h and the local pressures p_h . A condition defining the global pressure \bar{p}_h on cell facets is obtained by enforcing weak continuity of the numerical mass flux $\hat{\mathbf{u}}_h$ across cell facets

$$\sum_K \int_{\partial K} \hat{\mathbf{u}}_h \cdot \mathbf{n} \bar{q}_h d\Gamma - \int_{\partial \Omega} \bar{\mathbf{u}}_h \cdot \mathbf{n} \bar{q}_h d\Gamma = 0 \quad \forall \bar{q}_h \in \bar{Q}_h, \quad (29)$$

where $\bar{\mathbf{u}}_h \in \bar{W}_{h,g}$.

A local Galerkin approximation to the momentum balance (Eq. (11)) can be formulated as follows: find $\mathbf{u}_h \in W_h$ such that

$$\begin{aligned} \int_{\Omega} \frac{\partial \mathbf{u}_h}{\partial t} \cdot \mathbf{w}_h d\Omega - \sum_K \int_K \boldsymbol{\sigma}_h : \nabla \mathbf{w}_h d\Omega + \sum_K \int_{\partial K} \hat{\boldsymbol{\sigma}}_h \mathbf{n} \cdot \mathbf{w}_h d\Gamma \\ + \sum_K \int_{\partial K} 2\nu (\bar{\mathbf{u}}_h - \mathbf{u}_h) \cdot \nabla^s \mathbf{w}_h \mathbf{n} d\Gamma = \int_{\Omega} \mathbf{f} \cdot \mathbf{w}_h d\Omega \quad \forall \mathbf{w}_h \in W_h, \end{aligned} \quad (30)$$

given the external forcing \mathbf{f} , the kinematic viscosity ν , the facet velocity $\bar{\mathbf{u}}_h \in \bar{W}_{h,g}$ and the pressures $p_h \in Q_h$ and $\bar{p}_h \in \bar{Q}_h$. Furthermore, the momentum flux $\boldsymbol{\sigma}_h$ is given by

$$\boldsymbol{\sigma}_h = p_h \mathbf{I} - 2\nu \nabla^s \mathbf{u}_h, \quad (31)$$

and a numerical momentum flux $\hat{\boldsymbol{\sigma}}_h$ on cell facets is defined as

$$\hat{\boldsymbol{\sigma}}_h = \bar{p}_h \mathbf{I} - 2\nu \nabla^s \mathbf{u}_h - \frac{\alpha}{h_K} 2\nu (\bar{\mathbf{u}}_h - \mathbf{u}_h) \otimes \mathbf{n}, \quad (32)$$

where α is a penalty parameter, as is typical of interior penalty methods [29]. As with the pressure-stabilizing term, the penalty term is local in that neighboring cells do not directly interact with each other, but only via the facet functions.

Similar to the global continuity equation, Eq. (29), a global momentum equation is furnished, requiring the numerical momentum flux $\hat{\boldsymbol{\sigma}}_h$ to be weakly continuous across cell facets. This results in the constraint

$$\sum_K \int_{\partial K} \hat{\boldsymbol{\sigma}}_h \mathbf{n} \cdot \bar{\mathbf{w}}_h d\Gamma = \int_{\Gamma_N} \mathbf{h}_d \cdot \bar{\mathbf{w}}_h d\Gamma \quad \forall \bar{\mathbf{w}}_h \in \bar{W}_{h,0}, \quad (33)$$

with \mathbf{h}_d a given diffusive momentum flux at the boundary Γ_N .

Given the context of particle-mesh methods, it is important to elaborate upon the pressure stabilizing term β in Eq. (28) in some more detail. Substituting Eq. (28) in Eqs. (27) and (29), and setting $\bar{q}_h = 0$ and $q_h = 1$ on a cell $K \in \mathcal{T}$ leads to the local mass conservation statement

$$\int_K \nabla \cdot \mathbf{u}_h d\Omega = \int_{\partial K} \frac{\beta h_K}{\nu + 1} (\bar{p}_h - p_h) d\Gamma \quad \forall K \in \mathcal{T}. \quad (34)$$

In a mixed order case, setting $m = k - 1$, β can be set to zero [22, 28]. As shown in these references, this results in velocity fields \mathbf{u}_h that are pointwise divergence-free within a cell. However, since the velocity fields $\mathbf{u}_h \in W_h$ are not $H(\text{div})$ conforming, the facet normal velocity component is not pointwise continuous across cell facets. For the equal-order case (i.e. $m = k$) β must be positive [22, 28] which, according to Eq. (34), relaxes the incompressibility constraint in proportion to the stability parameter β . The resulting local mass conservation errors are, however, extremely small for values of β typically required to ensure stability [22].

Finally, an important difference with the fully Eulerian formulation in [22] is the absence of the advective flux terms since advection of the material quantities is done at the particle level. Hence, the resulting set of equations at the mesh becomes linear.

3.3. Particle-mesh projection

The operator $\mathcal{P}_E : V \rightarrow W_h$ in Eq. (16) projects the particle properties (i.e. the specific momentum carried by the particles) from the scattered set of Lagrangian particles onto W_h , that is, the space of piecewise-continuous basis functions defined on the mesh. To this end, an ℓ^2 -projection is adopted by minimizing the objective function

$$J := \sum_{p \in \mathcal{S}_t} \frac{1}{2} \|\mathbf{u}_h(\mathbf{x}_p(t), t) - \mathbf{v}_p(t)\|^2, \quad (35)$$

with respect to the mesh velocity field $\mathbf{u}_h(t) \in W_h$, where $\mathbf{v}_p(t) \in \mathcal{V}_t$ and $\mathbf{x}_p(t) \in \mathcal{X}_t$ are the velocity and position of particle p at time instant t , respectively. Furthermore, $\|\cdot\|^2$ denotes the square of the Euclidean

norm, i.e. $\|\mathbf{u}\|^2 = \mathbf{u} \cdot \mathbf{u}$.

265 Equating the variations δJ with respect to the variations $\delta \mathbf{u}_h$ to zero leads to

$$\sum_{p \in \mathcal{S}_t} (\mathbf{u}_h(\mathbf{x}_p(t), t) - \mathbf{v}_p(t)) \cdot \delta \mathbf{u}_h(\mathbf{x}_p(t)) = 0 \quad \forall \delta \mathbf{u}_h \in W_h. \quad (36)$$

This equation can be written as a summation of local equations on cells $K \in \mathcal{T}$: at time t , given the particle specific momentum $\mathbf{v}_p(t)$, find $\mathbf{u}_h(t) \in W_h$ such that

$$270 \quad \sum_K \sum_{p \in \mathcal{S}_t^K} (\mathbf{u}_h(\mathbf{x}_p(t), t) - \mathbf{v}_p(t)) \cdot \mathbf{w}_h(\mathbf{x}_p(t)) = 0 \quad \forall \mathbf{w}_h \in W_h, \quad (37)$$

replacing the variations $\delta \mathbf{u}_h$ with the local test functions $\mathbf{w}_h \in W_h$.

Since $\mathbf{u}_h \in W_h$ and $\mathbf{w}_h \in W_h$ are discontinuous across cell boundaries, Eq. (37) can be solved in a cellwise fashion. Hence, the mapping of the particle data to the mesh basis functions only involves the inversion
275 of small, local matrices. Eq. (37) has a regular solution if and only if the number of particles in a cell is bounded from below by the number of local basis functions.

For simplicial meshes, we note that the above presented ℓ^2 -projection onto the discontinuous HDG basis is similar to an MLS-reconstruction for specific choices of the basis and the particle weighting function in the latter approach, which is further detailed in Appendix A.

280 3.4. Mesh-particle projection

The mesh-particle projection $\mathcal{P}_L : W_h \rightarrow V$ in Eq. (10) concerns the update of the specific momentum carried by the particles. Starting from Eq. (35), the mesh-particle projection seeks to minimize the objective function J with respect to the particle field $\mathbf{v}_p(t) \in \mathcal{V}_t$, which leads to

$$285 \quad \sum_{p \in \mathcal{S}_t} (\mathbf{u}_h(\mathbf{x}_p(t), t) - \mathbf{v}_p(t)) \cdot \delta \mathbf{v}_p = 0 \quad \forall \delta \mathbf{v}_p \in \mathcal{V}_t. \quad (38)$$

Since this equation holds for arbitrary variations $\delta \mathbf{v}_p$, the particularly simple result for the semi-discrete particle update becomes

$$\mathbf{v}_p(t) = \mathbf{u}_h(\mathbf{x}_p(t), t) \quad \forall p \in \mathcal{S}_t. \quad (39)$$

290 The mesh-particle projection governed by Eq. (39) is not restricted to the mapping of the velocity $\mathbf{u}_h \in W_h$ to the particles only, but can be applied to project arbitrary fields in W_h (or Q_h for scalar quantities) onto the particles.

4. A fully discrete solution procedure

A fully discrete solution procedure is obtained by applying suitable time integration schemes to the
295 model components of the general method presented in Section 3.

Introducing the notation $\mathbf{x}_p^{n,n+1} = \mathbf{x}_p(t^{n,n+1})$ and $\mathbf{v}_p^{n,n+1} = \mathbf{v}_p(t^{n,n+1})$, the time integration algorithm on subinterval $I_n = [t^n, t^{n+1}]$ consists of the following consecutive steps:

1. *Particle advection*: $\mathbf{x}_p^n \rightarrow \mathbf{x}_p^{n+1}$; the particle position is updated in a Lagrangian manner using an advective velocity field, see Section 4.1.
- 300 2. *Particle-mesh projection*: $\mathbf{v}_p^n \rightarrow \mathbf{u}_h^{*,n}$; an intermediate velocity field $\mathbf{u}_h^{*,n}$ is constructed at the mesh from the particle velocities \mathbf{v}_p^n and the updated particle positions \mathbf{x}_p^{n+1} , see Section 4.2.
3. *Solution of the Stokes problem on the mesh*: $\mathbf{u}_h^{*,n} \rightarrow \mathbf{u}_h^{n+1}$; the intermediate velocity field $\mathbf{u}_h^{*,n}$ is corrected to account for the diffusive momentum flux and external forcing while enforcing the incompressibility constraint, see Section 4.3.
- 305 4. *Mesh-particle projection*: $(\mathbf{u}_h^{*,n}, \mathbf{u}_h^{n+1}) \rightarrow \mathbf{v}_p^{n+1}$; the particle velocity is updated using the solution for the velocity \mathbf{u}_h^{n+1} at the mesh, see Section 4.4.

The operator splitting approach is evident from the steps outlined above since the advection step at the particle level leads to an intermediate velocity field that needs to be corrected at the mesh level.

A careful formulation of the updates of the particle properties (steps 1 and 4) is crucial to minimize the associated splitting error and to achieve higher-order accuracy in time. The reason for this is that the particles retain the flow variables (i.e. specific momentum) between consecutive time steps, while the flow variables are not permanent to the mesh. Below, we will present a viable scheme that makes it possible to obtain second-order time accuracy.

4.1. Particle advection

315 Two issues have to be addressed regarding the advection of particles: first, the advective velocity must be determined and, second, a method for solving Eq. (26) must be formulated. It follows from Eq. (25) that the particle momentum itself is constant during this stage.

Owing to the HDG method, the velocity fields \mathbf{u}_h on the mesh approximate the divergence-free constraint accurately in a local sense and, as argued in Section 3.2, can be made pointwise divergence-free within a cell for the mixed order case. Exploiting this feature, a judicious choice for the advective velocity $\tilde{\mathbf{v}}(\mathbf{x}, t)$ in Eq. (26) is to use the mesh velocity field $\mathbf{u}_h \in W_h$ frozen at the old time level t^n , i.e.

$$\tilde{\mathbf{v}}(\mathbf{x}_p(t), t^n) = \mathbf{u}_h(\mathbf{x}_p(t), t^n), \quad (40)$$

where $\mathbf{x}_p(t) \in \mathcal{X}_t$ denotes the particle positions at time instant $t \in [t^n, t^{n+1}]$.

Any time stepping scheme which is sufficiently accurate can be used for integrating Eq. (26) in time. In this study, a three step, third-order accurate Runge-Kutta scheme is used [30].

During the advection step, particles have to enter the domain at inflow boundaries. To this end, particles are seeded in the cells contiguous to the inflow boundaries keeping the number of particles constant in these

cells. To remain consistent with the boundary conditions in Eqs. (8-9), the momenta of the inserted particles are interpolated from the corresponding values imposed by the boundary conditions.

330 4.2. Particle-mesh mapping

In a time-discrete setting, the local minimization problem of Eq. (37) reads as follows: given the velocities $\mathbf{v}_p^n \in \mathcal{V}_t$ and positions $\mathbf{x}_p^{n+1} \in \mathcal{X}_t$, find the intermediate velocity field $\mathbf{u}_h^{*,n} \in W_h$ such that

$$\sum_K \sum_{S_t^K} (\mathbf{u}_h^{*,n}(\mathbf{x}_p^{n+1}) - \mathbf{v}_p^n) \cdot \mathbf{w}_h(\mathbf{x}_p^{n+1}) = 0 \quad \forall \mathbf{w}_h \in W_h. \quad (41)$$

335 This fully defines the discretization of the operator \mathcal{P}_E in Eq. (16).

4.3. Solving the equations at the mesh

Using the backward Euler method, with time step size $\Delta t^n = t^{n+1} - t^n$, the following time-discrete functionals are solved for $\mathbf{U}_h^{n+1} := (\mathbf{u}_h^{n+1}, \bar{\mathbf{u}}_h^{n+1}, p_h^{n+1}, \bar{p}_h^{n+1})$.

The time-discrete functional for the local momentum balance, Eq. (30), reads

$$\begin{aligned} F_m(\mathbf{U}_h^{n+1}, \mathbf{w}_h) &:= \int_{\Omega} \frac{\mathbf{u}_h^{n+1} - \mathbf{u}_h^{*,n}}{\Delta t^n} \cdot \mathbf{w}_h d\Omega - \sum_K \int_K \boldsymbol{\sigma}_h^{n+1} : \nabla \mathbf{w}_h d\Omega \\ &+ \sum_K \int_{\partial K} \hat{\boldsymbol{\sigma}}_h^{n+1} \mathbf{n} \cdot \mathbf{w}_h d\Gamma + \sum_K \int_{\partial K} 2\nu (\bar{\mathbf{u}}_h^{n+1} - \mathbf{u}_h^{n+1}) \cdot \nabla^s \mathbf{w}_h \mathbf{n} d\Gamma - \int_{\Omega} \mathbf{f}^{n+1} \cdot \mathbf{w}_h d\Omega. \end{aligned} \quad (42)$$

The functional for the global momentum balance, Eq. (33), becomes

$$\bar{F}_m(\mathbf{U}_h^{n+1}, \bar{\mathbf{w}}_h) := \sum_K \int_{\partial K} \hat{\boldsymbol{\sigma}}_h^{n+1} \mathbf{n} \cdot \bar{\mathbf{w}}_h d\Gamma - \int_{\Gamma_N} \mathbf{h}^{n+1} \cdot \bar{\mathbf{w}}_h d\Gamma. \quad (43)$$

The functional for the local continuity equation (27) reads

$$F_c(\mathbf{U}_h^{n+1}, q_h) := \sum_K \int_K \mathbf{u}_h^{n+1} \cdot \nabla q_h d\Omega - \sum_K \int_{\partial K} \hat{\mathbf{u}}_h^{n+1} \cdot \mathbf{n} q_h d\Gamma, \quad (44)$$

And, finally, the functional for the global continuity equation (28) is given by

$$\bar{F}_c(\mathbf{U}_h^{n+1}, \bar{q}_h) := \sum_K \int_{\partial K} \hat{\mathbf{u}}_h^{n+1} \cdot \mathbf{n} \bar{q}_h d\Gamma - \int_{\partial\Omega} \bar{\mathbf{u}}_h^{n+1} \cdot \mathbf{n} \bar{q}_h d\Gamma, \quad (45)$$

350 Defining

$$F(\mathbf{U}_h^{n+1}, \mathbf{W}_h) := F_m(\mathbf{U}_h^{n+1}, \mathbf{w}_h) + \bar{F}_m(\mathbf{U}_h^{n+1}, \bar{\mathbf{w}}_h) + F_c(\mathbf{U}_h^{n+1}, q_h) + \bar{F}_c(\mathbf{U}_h^{n+1}, \bar{q}_h), \quad (46)$$

with $\mathbf{W}_h := (\mathbf{w}_h, \bar{\mathbf{w}}_h, q_h, \bar{q}_h)$, results in the following fully discrete system to be solved at the mesh: given $\mathbf{u}_h^{*,n} \in W_h$, the forcing term \mathbf{f}^{n+1} , the boundary flux term \mathbf{h}_d^{n+1} , and the viscosity ν , find $\mathbf{U}_h^{n+1} \in W_h \times \bar{W}_{h,0} \times Q_h \times \bar{Q}_h$, such that

$$355 F(\mathbf{U}_h^{n+1}, \mathbf{W}_h) = 0 \quad \forall \mathbf{W}_h \in W_h \times \bar{W}_{h,0} \times Q_h \times \bar{Q}_h. \quad (47)$$

4.4. Mesh-particle projection

The particle momentum is updated by mapping the acceleration field from the background mesh to the particles using the two-level θ -method

$$\mathbf{v}_p^{n+1} = \mathbf{v}_p^n + \Delta t \left((1 - \theta) \dot{\mathbf{v}}_p^n + \theta \dot{\mathbf{v}}_p^{n+1} \right) \quad \forall p \in \mathcal{S}_t, \quad (48)$$

in which $\theta \in [1/2, 1]$ is a parameter and $\dot{\mathbf{v}}_p^n$ and $\dot{\mathbf{v}}_p^{n+1}$ are the particle accelerations at time level t^n and t^{n+1} , respectively. The particle acceleration is obtained from the acceleration field on the mesh using the projection defined in Eq. (39). For the particle acceleration at time level t^n this gives for instance

$$\dot{\mathbf{v}}_p^n = \dot{\mathbf{u}}_h^n(\mathbf{x}_p^n) \quad \forall p \in \mathcal{S}_t, \quad (49)$$

where the acceleration field $\dot{\mathbf{u}}_h^n \in W_h$ is given by $\dot{\mathbf{u}}_h^n = (\mathbf{u}_h^n - \mathbf{u}_h^{*,n-1}) / \Delta t^n$.

Choosing $\theta = 1$ in Eq. (48) results in the first-order accurate backward Euler method, whereas $\theta = 1/2$ yields the second-order accurate Crank-Nicolson method. Setting $\theta = 1/2$ in combination with the backward Euler discretization of Eq. (47) yields overall second-order time accuracy, see Appendix B. The accuracy of the time stepping scheme is verified in Section 5 by means of a numerical error and grid convergence analysis.

4.5. Algorithmic aspects

In order to appreciate and understand the model formulation, the implications of the coupling between the Lagrangian particles and the Eulerian mesh are briefly discussed, and the attractive features of combining an HDG approach with ℓ^2 -projections between particles and mesh are highlighted. The aspects identified below are further explored in Section 5 by means of different validation and benchmark tests.

Central to the approach is the decoupling between the advection step, done at particle level, and a Stokes step, performed at the mesh level. Using this operator splitting approach, the nonlinear advection term is eliminated from the problem, thus avoiding the need for additional stabilization mechanisms in the advective limit. The coupling between the particles and the mesh is established by means of two projection steps, which are casted in a generic variational framework.

The particle-mesh projection step bears some similarities with the (weighted) moving least-squares approach adopted in, e.g., [13, 14]. More precisely, Appendix A shows that for a specific choice of the basis and the particle weighting function in an MLS-reconstruction, this approach coincides with the presented (local) ℓ^2 -projections. However, by adopting the presented ℓ^2 -projections of the particle properties onto the discontinuous basis functions employed by the HDG method, the particle-mesh projection step requires the inversion of a small matrix only once per cell. Furthermore, the particle influence remains strictly localized to its hosting cell, which is attractive from an implementation and parallelization perspective.

Two considerations further motivate why the HDG method is the Stokes solver of choice. Firstly, this method was proven to have excellent local mass conservation properties [22]. In a particle-mesh context this

is a highly attractive feature, since the particles can be advected through velocity fields which are nearly locally divergence-free (for the equal order case) or pointwise divergence-free within a cell (for the mixed order case). As discussed in the introduction, this is a prerequisite for maintaining a uniform particle distribution. Secondly, its formulation allows for a static condensation procedure by eliminating the local unknowns in favor of the global unknowns. Since $\bar{\mathbf{u}}_h$ and \bar{p}_h are chosen to be continuous on facets (i.e. $k, m \geq 1$ and $\bar{Q}_h \in H^{1/2}$), the resulting global system has the same number of degrees of freedom as a continuous method based on the same polynomial orders.

The update of the specific momentum of the particles, as proposed in Section 4.4, bears some resemblance with the approach typical to FLIP and MPM in which the particle properties are updated using the corresponding increments on the mesh. However, we strictly avoid the heuristic damping term in the mesh-particle projection which is often used in the aforementioned methods to enhance stability for advection-dominated problems (see e.g. [5, 9, 13]).

Finally, while the HDG method for the Navier-Stokes equations conserves momentum exactly [22], this desirable property is not inherited by the proposed particle-mesh algorithm as the ℓ^2 -projection from the particles to the mesh is not momentum conserving. However, this auxiliary step warrants a consistent approximation of the momentum contained in a cell, that is, momentum is conserved if the number of particles tends to infinity and the particle distribution is uniform.

5. Numerical examples

This section presents various numerical examples to demonstrate the model capabilities. First of all, the convergence and accuracy of the proposed method are studied by means of a numerical error and grid convergence analysis. To this end, two test cases are considered. The Poiseuille flow problem is used to study the spatial convergence for a problem converging to a steady state. The Taylor-Green flow problem is used to investigate the accuracy of the time stepping scheme and to assess the momentum error introduced by the ℓ^2 -projections. This test case is also used to assess the quality of the particle distribution.

By presenting results for the flow over a backward facing step and for the flow around a cylinder, the second part of this section is dedicated to demonstrate the capabilities of the developed method for realistic problems arising in engineering applications. Of special interest are the quality of the particle distribution and the accuracy of the computed dynamic parameters.

All tests presented in this section are performed for domains $\Omega \in \mathbb{R}^2$ and assume a unit density. The time domains of interest are uniformly partitioned using constant time step sizes Δt . Furthermore, equal-order polynomial basis functions are used, that is: $k = m \geq 1$ and the numerical parameters α and β are set to $\alpha = 6k^2$ and $\beta = 10^{-6}$, respectively, in all computations. The governing equations at the mesh are solved using tools from the FEniCS project [31].

5.1. Convergence study: Poiseuille flow

425 In order to study spatial convergence, plane Poiseuille flow is considered, simulating the incompressible viscous flow between two parallel plates extending to infinity. Starting from rest, the flow gradually develops towards a steady state under the influence of a constant axial body force \mathbf{F} . The channel is modeled in the x - y plane, where the x -axis points in the direction of the flow and the plates are located at $y = \pm d$. The flow is periodic in the x -direction and the no-slip boundary condition $\mathbf{u} = \mathbf{0}$ is imposed at $y = \pm d$, the
430 respective locations of the plates.

The transient solution of the axial velocity $u_x(y, t)$ is given by the series expansion [32]

$$u_x(y, t) = \frac{|\mathbf{F}|}{2\nu}(d^2 - y^2) - \sum_{n=0}^{\infty} \frac{(-1)^n 16d^2 |\mathbf{F}|}{\nu\pi^3(2n+1)^3} \cos\left(\frac{(2n+1)\pi y}{2d}\right) \exp\left(-\frac{(2n+1)^2\pi^2\nu t}{4d^2}\right). \quad (50)$$

For $t \rightarrow \infty$ the exponential term at the right-hand side tends to zero, resulting in the steady-state solution

$$u_x(y) = \frac{|\mathbf{F}|}{2\nu}(d^2 - y^2) = U \left(1 - \frac{y^2}{d^2}\right), \quad (51)$$

435 where $U = |\mathbf{F}|d^2/2\nu$ is the steady-state centerline velocity.

The model domain is given by $\Omega = [0, 1] \times [-0.25, 0.25]$. The kinematic viscosity is set to $\nu = 10^{-3}$, the body force $\mathbf{F} = (F_x, 0)^\top$ is chosen such that the Reynolds number $Re = U(2d)/\nu$ equals 200. A coarse, regular triangular mesh is constructed using $(10 \times 5 \times 2)$ cells with a cell size $h_K = 0.1\sqrt{2}$. The coarse mesh is refined three times where the finest mesh contains $(80 \times 40 \times 2)$ cells with $h_K = 0.0125\sqrt{2}$. Particles are
440 randomly distributed in the domain, assigning an average of 50 particles per cell initially. This number is also found in literature, where typically 20 to 50 particles per cell are used [2, 6, 33, 34]. The number of particles per cell is kept constant upon mesh refinement. The CFL-number is defined as:

$$\text{CFL} = \frac{U\Delta t}{h_K}. \quad (52)$$

Furthermore, the value for θ in Eq. (48) is set to 1/2.

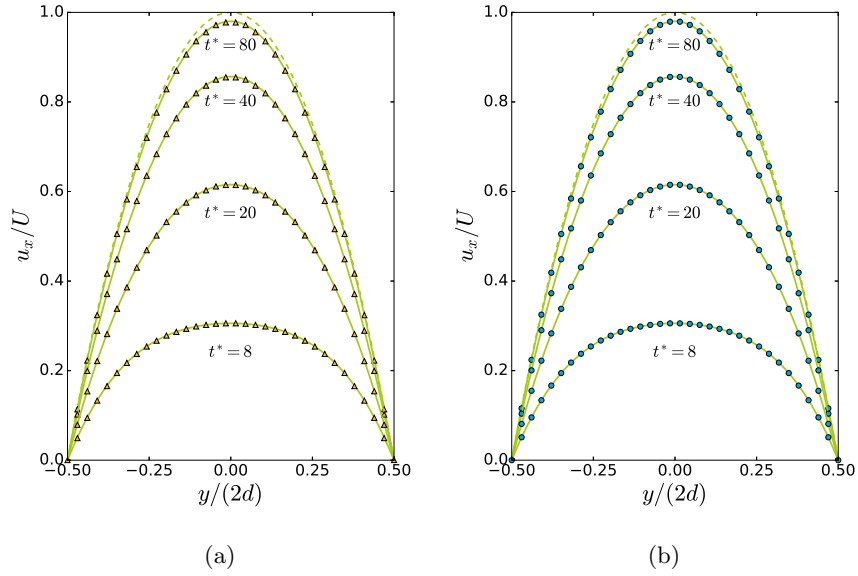


Figure 1: Poiseuille flow: non-dimensional flow velocity profiles at various dimensionless time instants $t^* = tU/2d$ for $Re = 200$ using polynomial orders (a) $k = 1$ (\triangle) and (b) $k = 2$ (\circ); also shown are the analytical solutions (solid) including the steady-state solution for $t \rightarrow \infty$ (dashed).

445 The discrete solutions of the velocity profile at various dimensionless time instants $t^* = tU/2d$ using a mesh of $(40 \times 20 \times 2)$ cells and a corresponding time step size $\Delta t = 0.125$ ($CFL \approx 1$) are shown in Fig. 1 for piecewise-linear basis functions (i.e. $k = 1$) and piecewise-quadratic basis functions (i.e. $k = 2$). Both for the linear - and the quadratic basis functions the results match closely with the analytical solution.

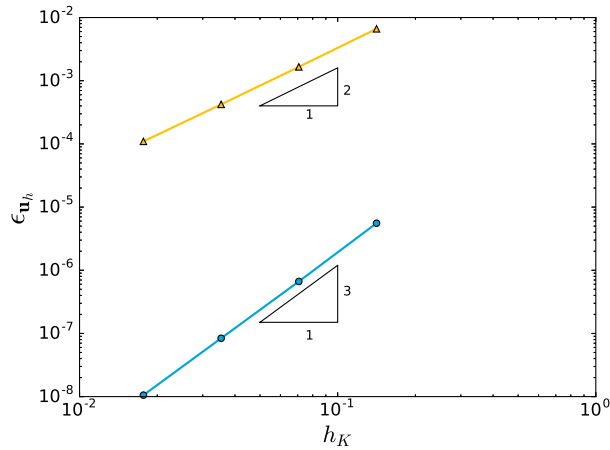


Figure 2: Poiseuille flow: L^2 -error norm of \mathbf{u}_h as function of the characteristic cell size h_K at $t^* = 80$ for polynomial orders $k = 1$ (\triangle) and $k = 2$ (\circ).

The spatial convergence of the method in the time-dependent case is studied using a small time step (corresponding to a CFL-number of approximately 0.4) in order to diminish the time stepping error. The velocity error at time $t^* = 80$ is examined via the L^2 -error norm $\epsilon_{\mathbf{u}_h} = \|\mathbf{u} - \mathbf{u}_h\|_{L^2(\Omega)}$, which is plotted in Fig. 2 for polynomial orders $k = 1$ and $k = 2$. The errors and the resulting rates of convergence are also summarized in Table 1. The results show optimal spatial convergence rates of order $k + 1$, indicating that the spatial convergence rate is not affected by the particle-mesh operator splitting.

Table 1: Poiseuille flow: convergence of the L^2 -error norm of \mathbf{u}_h at $t^* = 80$.

		$k = 1$		$k = 2$	
h_K	Δt	$\epsilon_{\mathbf{u}_h}$	order	$\epsilon_{\mathbf{u}_h}$	order
$0.1\sqrt{2}$	0.2	6.63e-3	-	5.55e-6	-
$0.05\sqrt{2}$	0.1	1.63e-3	2.0	6.65e-7	3.06
$0.025\sqrt{2}$	0.05	4.21e-4	1.97	8.38e-8	2.99
$0.0125\sqrt{2}$	0.025	1.10e-4	1.94	1.06e-8	2.99

5.2. Convergence study: Taylor-Green flow

The Taylor-Green problem features a periodic sequence of decaying vortices. On a rectangular domain with horizontal dimensions L_x and L_y , closed analytical expressions for the velocity and the pressure are given by, respectively,

$$\mathbf{u}(\mathbf{x}, t) = U \exp(-2\nu\pi^2 t) (-\cos(k_x x) \sin(k_y y), \sin(k_x x) \cos(k_y y))^\top, \quad (53)$$

$$p(\mathbf{x}, t) = \frac{1}{4} \exp(-4\nu\pi^2 t) (\cos(2k_x x) + \cos(2k_y y)), \quad (54)$$

in which U is the initial velocity amplitude, ν is the kinematic viscosity, and $k_x = 2\pi/L_x$ and $k_y = 2\pi/L_y$ are wave numbers in the x - and y -direction, respectively.

Since only an initial condition needs to be imposed, the Taylor-Green test is particularly suited to determine the accuracy of the time integration method. Due to the absence of body forces and boundary conditions, the test is also useful to analyze the momentum error. First and foremost, however, the Taylor-Green problem is used to assess the quality of the particle advection algorithm. In particular, the presence of stagnation points can lead to a poor particle distribution, as observed in other Lagrangian particle methods (see e.g. [15, 21]). Maintaining a high-quality particle distribution is imperative since the occurrence of clusters or voids would compromise the resolution of the specific momentum provided by the particles.

The test uses a square domain $\Omega = [-1, 1] \times [-1, 1]$, so that $L_x = L_y = 2$, and a time interval of interest $I = [0, 2]$. The initial velocity amplitude U is set to 1 for all computations, and the kinematic viscosity ν is either set to $2 \cdot 10^{-2}$ or $2 \cdot 10^{-3}$, resulting in Reynolds numbers of $Re = UL/\nu = 100$ and $Re = 1000$,

respectively. Similar to the Poiseuille flow test, 50 particles are assigned on average per cell initially. The CFL-number is defined as in Eq. (52), with U the initial velocity amplitude from Eq. (53).

5.2.1. Particle distribution

A time dependent measure $\delta S(t)$ for the uniformity of the particle distribution is given by [35]

$$\delta S(t) = \frac{1}{|\mathcal{T}|} \sum_K \left| \frac{|\mathcal{S}_t^K| - \bar{\mathcal{S}}_0^K}{\bar{\mathcal{S}}_0^K} \right|, \quad (55)$$

in which $|\mathcal{T}|$ is the number of cells, $\bar{\mathcal{S}}_0^K = |\mathcal{S}_0|/|\mathcal{T}|$ is the average number of particles initially assigned per cell, and $|\mathcal{S}_t^K|$ is the number of particles in cell K at time t . The time dependent measure defined by Eq. (55) has two contributions: a probabilistic one due to the random particle position initialization and a deterministic one due to the particle advection (in literature also termed ‘bias error’ [35]). In order to study the isolated effect of the deterministic error due to the particle advection, the maximum absolute deviation and the standard deviation of the time series Eq. (55) are respectively defined as

$$\epsilon_{\delta S, \infty} = \max_{n=0, N_t} |\delta S(t^n) - \overline{\delta S}|, \quad (56)$$

$$\epsilon_{\delta S, \sigma} = \sqrt{\frac{1}{N_t} \sum_{n=0}^{N_t} (\delta S(t^n) - \overline{\delta S})^2}, \quad (57)$$

where $\overline{\delta S}$ denotes the mean of the time series, and N_t denotes the number of entries in the time series.

Furthermore, the error in the local mass conservation (Eq. (34)) is quantified by

$$\epsilon_{\nabla} = \left(\sum_K \int_K (\nabla \cdot \mathbf{u}_h)^2 d\Omega \right)^{1/2}. \quad (58)$$

The errors defined by Eq. (56), Eq. (57) and Eq. (58) are plotted in Fig. 3 for time $t = 5$, a CFL-number of 0.25, and a Reynolds number of 1000. Furthermore, polynomial orders $k = 1$ and $k = 2$ are used and θ is set to 1/2. Characteristic length scales for the mesh and time step sizes are similar to those listed in Table 2. For comparison, results obtained for a Taylor-Hood method with a continuous piecewise-quadratic velocity field and a continuous piecewise-linear pressure field (TH 2-1) are also included in Fig. 3.

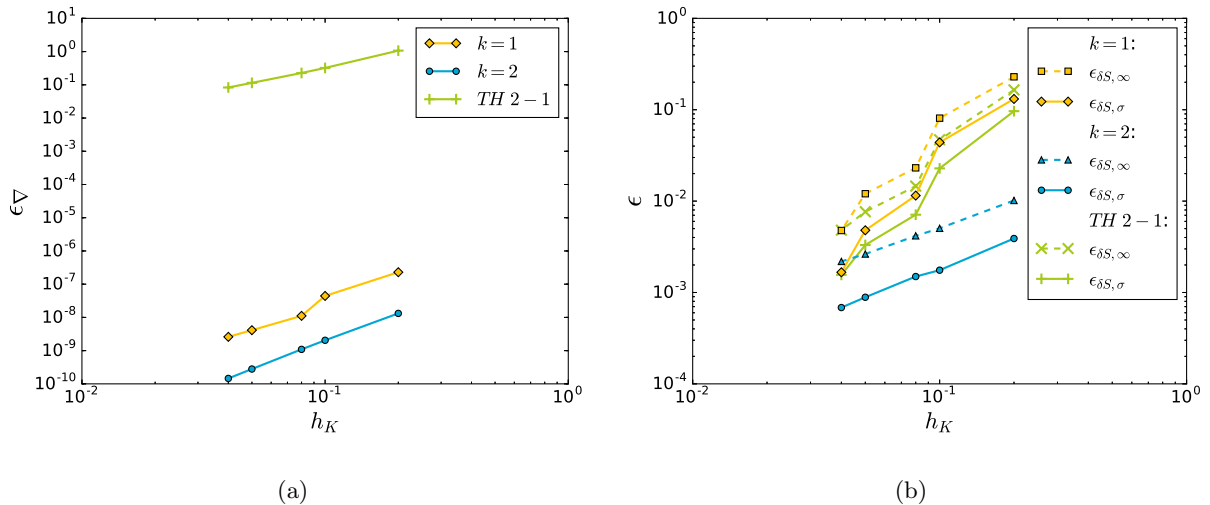
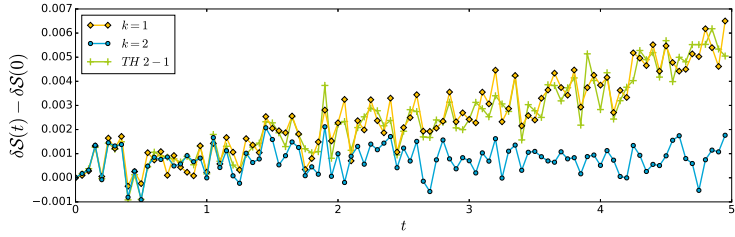
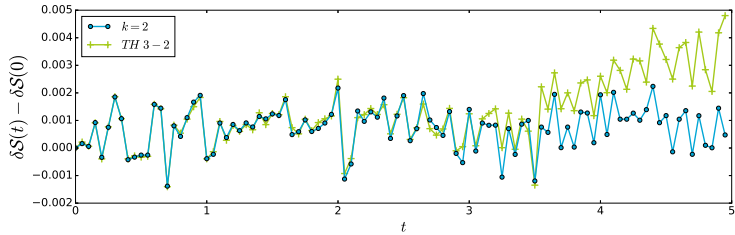


Figure 3: Taylor-Green flow: divergence errors (a) and particle distribution errors (b) at time $t = 5$ versus cell size h_K for $k = 1$ and $k = 2$, compared with a Taylor-Hood method (TH 2-1). Presented results are for a CFL-number of 0.25, a Reynolds number of 1000, and $\theta = 1/2$.

The local divergence errors in the HDG method are very small indeed, whereas the local divergence error for the Taylor-Hood method is orders of magnitude larger. For both polynomial orders (HDG) and the Taylor-Hood method, the particle distribution error converges consistently when increasing the spatial resolution (i.e. refining the mesh while keeping the average number of particles per cell constant). However, for the coarse-resolution tests, the particle distribution error is much smaller when using quadratic polynomials ($k = 2$) than it is when using linear polynomials ($k = 1$) or a Taylor-Hood method. For the high-resolution tests, the particle distribution errors appear to be comparable, irrespective of the polynomial order or method. However, plotting the timeseries $\delta S(t) - \delta S(0)$ for the test with $h_K = 0.04$ in Fig. 4 reveals the persistence of an important difference: for the linear polynomials (i.e. $k = 1$) and a Taylor-Hood method (TH 2-1), the particle distribution error ($\delta S(t) - \delta S(0)$) gradually increases over time, see Fig. 4a. Using higher polynomial orders in the Taylor-Hood method at best delays this issue. This is shown in Fig. 4b for a test with $h_K = 0.04$ and a Reynolds number of 10^6 , using a Taylor-Hood method with a continuous piecewise-cubic velocity field and a continuous piecewise-quadratic pressure field (TH 3-2). Ultimately, the particle distribution for the TH 3-2 method starts to deviate from the initially uniform distribution, giving an increasing particle distribution error. For longer computations, this will inevitably lead to empty cells (i.e. cells not containing any particles), thus corrupting the simulation. However, for the HDG method with quadratic polynomials (i.e. $k = 2$) the particle distribution error does not grow, irrespective of the Reynolds number.



(a)



(b)

Figure 4: Taylor-Green flow: time history of the particle distribution error for the HDG method with $k = 1$, $k = 2$, a Taylor-Hood method (TH 2-1) and $Re = 1000$ (a), and for the HDG method with $k = 2$, a Taylor-Hood method (TH 3-2) and $Re = 1e6$ (b); $h_K = 0.04$ and $\theta = 1/2$.

The practical implications of the aforementioned observations are illustrated in Fig. 5 in which the
515 particle distributions are plotted for different combinations of element type and polynomial order for the
test case with $h_K = 0.20$ and a Reynolds number of 1000. Using the HDG method with a polynomial order
 $k = 2$, even on this coarse mesh a uniform particle distribution is maintained, Fig. 5b . However, the HDG
method in combination with a polynomial order $k = 1$ results in a non-uniform particle distribution, Fig. 5a.
An explanation for the drastic improvement of the results for the HDG method with $k = 2$ over the HDG
520 method with $k = 1$ can be found in terms of the inter-element continuity of the velocity field $\mathbf{u}_h \in W_h$.
Using a quadratic basis for the facet pressures (with $m = k = 2$ in Eq. (20)), the pressure dofs placed at
the facet midpoints offer improved control over the facet-normal velocity component compared to the case
 $k = 1$ (with $m = k = 1$), leading to an improved inter-element continuity of the advective velocity field.
The non-uniformity in the particle distribution is also observed for the cases using the Taylor-Hood method
525 and is especially pronounced for the TH 2-1 case, see Fig. 5c. Albeit the particle distribution significantly
improves for the TH 3-2 case compared to the TH 2-1 case, the non-uniformity in the particle distributions
becomes clearly visible for longer simulation runtimes, Fig. 5d. Since inter-element continuity is inherent
from the choice of the velocity function spaces, this behavior is attributed to the local (i.e. cellwise)
divergence error in the Taylor-Hood method, see Fig. 3a.

In conclusion, it seems imperative to satisfy two criteria for maintaining a uniform particle distribution in
530 incompressible flows. Firstly, the velocity field by which the particles are advected has to be locally (or

pointwise) divergence-free, a condition which is extremely accurately met by the HDG method, see Fig. 3a. Secondly, the discrete velocity field should have a sufficient inter-element continuity. This, intuitively, can be achieved by using a higher-order polynomial basis (i.e. $k, m > 1$) in the HDG method. By satisfying these two criteria, a uniform particle distribution is maintained over time, even near stagnation points, and no additional particle shifting techniques or velocity field reconstruction techniques are required.

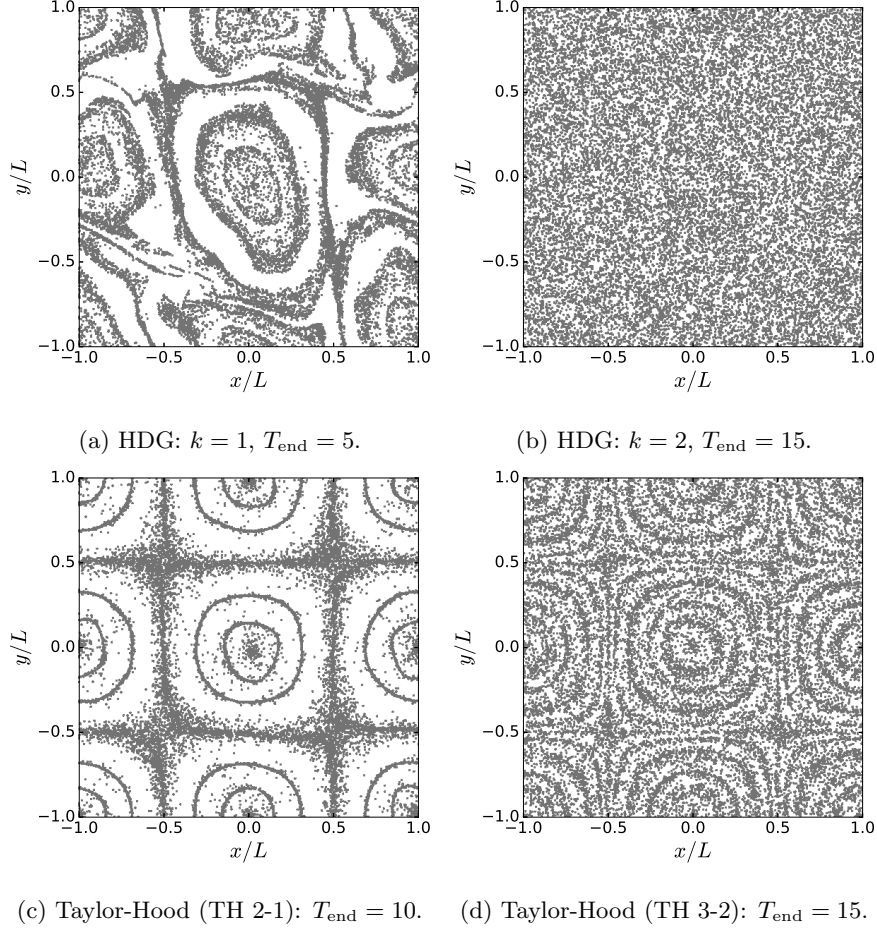


Figure 5: Taylor-Green flow: particle distributions at $t = T_{\text{end}}$ for different combinations of element type and polynomial order; $h_K = 0.20$, $Re = 1000$, $\theta = 1/2$.

5.2.2. Convergence tests

The convergence rates for the velocity and pressure errors are assessed for polynomial orders $k = 1$ and $k = 2$, by keeping the CFL-number equal to 0.25 while refining the mesh and decreasing the time step size. The model settings are summarized in Table 2. The centerline velocities and pressures at $t = 2$ for $h_K = 0.1$ m, $k = 2$ and $\Delta t = 0.025$ are plotted in Fig. 6, for Reynolds numbers $Re = 100$ and $Re = 1000$. From this figure, it follows that updating the particle velocities (Eq. (48)) using the backward Euler scheme

($\theta = 1$) results in numerical damping. However, when using the Crank-Nicolson scheme ($\theta = 1/2$) this damping is absent and accurate results for the velocity - and pressure distributions are obtained for moderate and relatively high Reynolds numbers.

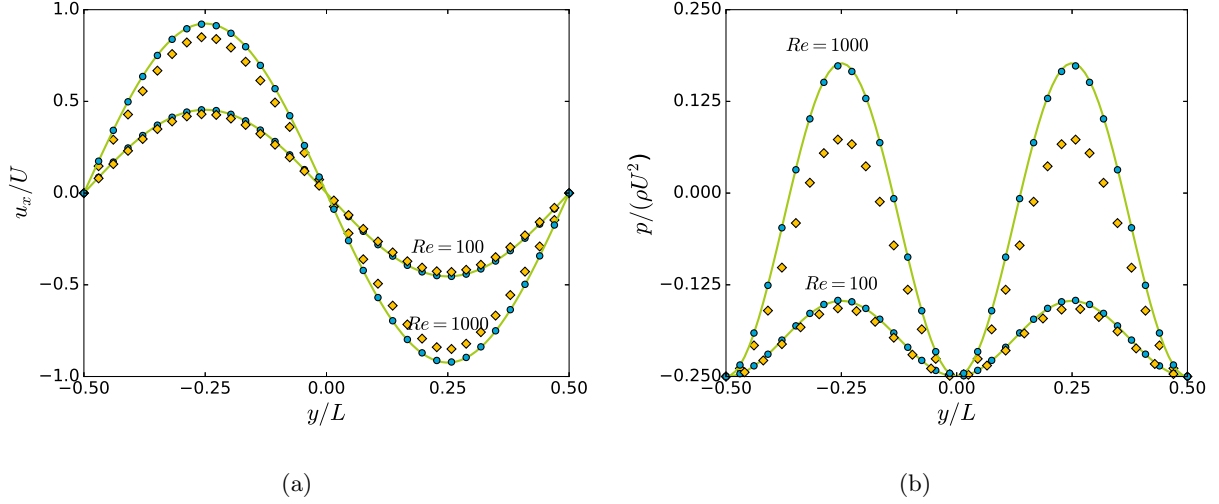


Figure 6: Taylor-Green flow: normalized velocities (a) and normalized pressures (b) along the central y -axis at $t = 2$ for different Reynolds numbers using polynomial order $k = 2$; shown are the results for $\theta = 1$ (\diamond), $\theta = 1/2$ (\circ) and the corresponding analytical solutions (solid).

In order to study the convergence of the L^2 -error norms of the pressure (i.e. $\epsilon_{p_h} = \|p - p_h\|_{L^2(\Omega)}$) and the velocity (i.e. $\epsilon_{\mathbf{u}_h} = \|\mathbf{u} - \mathbf{u}_h\|_{L^2(\Omega)}$), the Taylor-Green test is run on five different regular triangular meshes with characteristic cell sizes h_K ranging from 0.04 to 0.2, using corresponding time step sizes Δt ranging from 0.01 to 0.05, respectively. The results are tabulated in Table 2 and plotted in Fig. 7. For brevity, only the results for a Reynolds number of 1000 are given, noting that all conclusions are equally valid for the case $Re = 100$.

Clearly, the overall accuracy is reduced to first-order when using $\theta = 1$, irrespective of the polynomial order of the spatial discretization. This result is expected, since the truncation error of the time stepping scheme is dominant over the spatial errors. Using $\theta = 1/2$, a consistent second-order overall convergence is obtained for a polynomial order $k = 2$. For the polynomial order $k = 1$, large variations in convergence rates are observed between consecutive resolution refinements. This is probably related to the particle distribution, being less uniform for $k = 1$ as shown above. Note for example the similar pattern observed in the particle distribution error (Fig. 3b) and in the convergence of the pressure error (Fig. 7b) for $k = 1$ and $\theta = 1/2$. These results clearly demonstrate that maintaining a uniform particle distribution is essential for obtaining accurate results. This prerequisite is met if a polynomial order $k = 2$ is used in combination with a Crank-Nicolson update (i.e. $\theta = 1/2$) of the particle velocities, giving second-order overall convergence rates.

Table 2: Taylor-Green flow: overview of model runs with the associated errors $\epsilon_{\mathbf{u}_h}$ and ϵ_{p_h} at time $t = 2$ for different polynomial orders and different values for θ ; $Re = 1000$.

		$k = 1$				$k = 2$				
h_K	Δt	$\epsilon_{\mathbf{u}_h}$	Order	ϵ_{p_h}	Order	$\epsilon_{\mathbf{u}_h}$	Order	ϵ_{p_h}	Order	
$\theta = 1.0$	0.20	0.05	$2.64e-1$	—	$3.75e-1$	—	$2.26e-1$	—	$3.42e-1$	—
	0.10	0.025	$1.34e-1$	0.97	$2.12e-1$	0.82	$1.31e-1$	0.79	$2.15e-1$	0.67
	0.08	0.02	$1.08e-1$	0.97	$1.76e-1$	0.84	$1.07e-1$	0.90	$1.79e-1$	0.81
	0.05	0.0125	$6.99e-2$	0.92	$1.19e-1$	0.83	$7.06e-2$	0.88	$1.22e-1$	0.82
	0.04	0.01	$5.64e-2$	0.96	$9.76e-2$	0.89	$5.72e-2$	0.94	$1.00e-1$	0.89
$\theta = 0.5$	0.20	0.05	$8.79e-2$	—	$7.10e-2$	—	$1.55e-2$	—	$9.76e-3$	—
	0.10	0.025	$1.15e-2$	2.94	$7.35e-3$	3.27	$3.45e-3$	2.17	$2.63e-3$	1.89
	0.08	0.02	$5.72e-3$	3.12	$4.68e-3$	2.02	$2.17e-3$	2.08	$1.68e-3$	2.00
	0.05	0.0125	$1.72e-3$	2.55	$3.89e-3$	0.39	$8.16e-4$	2.08	$6.17e-4$	2.13
	0.04	0.01	$1.19e-3$	1.64	$2.91e-3$	1.30	$5.17e-4$	2.04	$3.68e-4$	2.31

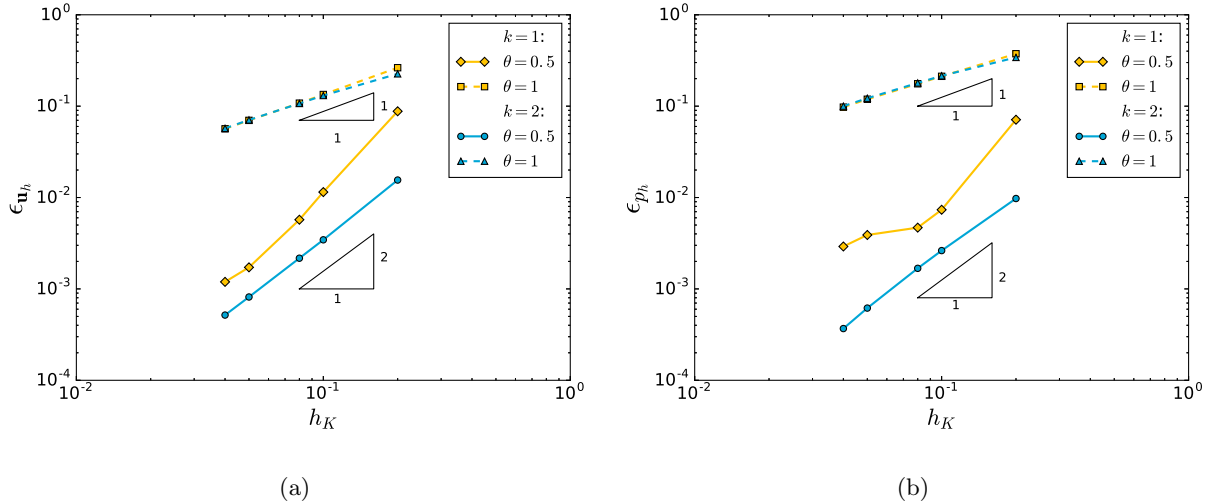


Figure 7: Taylor-Green flow: L^2 -error norms of velocity (a) and pressure (b) at time $t = 2$ versus the cell size h_K (with constant CFL-number) for $Re = 1000$ and different values of θ . Detailed results are given in Table 2.

5.2.3. Momentum conservation error

The results of the convergence tests demonstrate that the method is accurate in terms of the velocity - and pressure distributions. However, this does not yet mean that the method is also conservative (an issue which is often ignored in the particle-mesh literature). Since the Stokes solver was shown to conserve momentum exactly [22], momentum conservation errors are a result of the particle-mesh interactions only.

To this end, a mesh-related measure for the momentum conservation error is defined as

$$\epsilon_m = \left| \sum_K \int_K (\mathbf{u}_h(t) - \mathbf{u}_h(0)) \, d\Omega \right|. \quad (59)$$

570 The momentum conservation error at time $t = 2$ is plotted in Fig. 8 for different polynomial orders k , and $Re = 100$ and $Re = 1000$. Apart from the Reynolds number, the model settings are equal to those presented in Table 2. The superiority of the results when using polynomials of order $k = 2$ is clear, with momentum conservation errors being typically $\mathcal{O}(10 - 100)$ smaller compared to those observed for polynomials of order $k = 1$. For $k = 2$ the global momentum conservation errors, as defined by Eq. (59), are small and quickly
575 decrease upon mesh refinement, especially when using $\theta = 1/2$. Nevertheless, momentum is not conserved exactly.

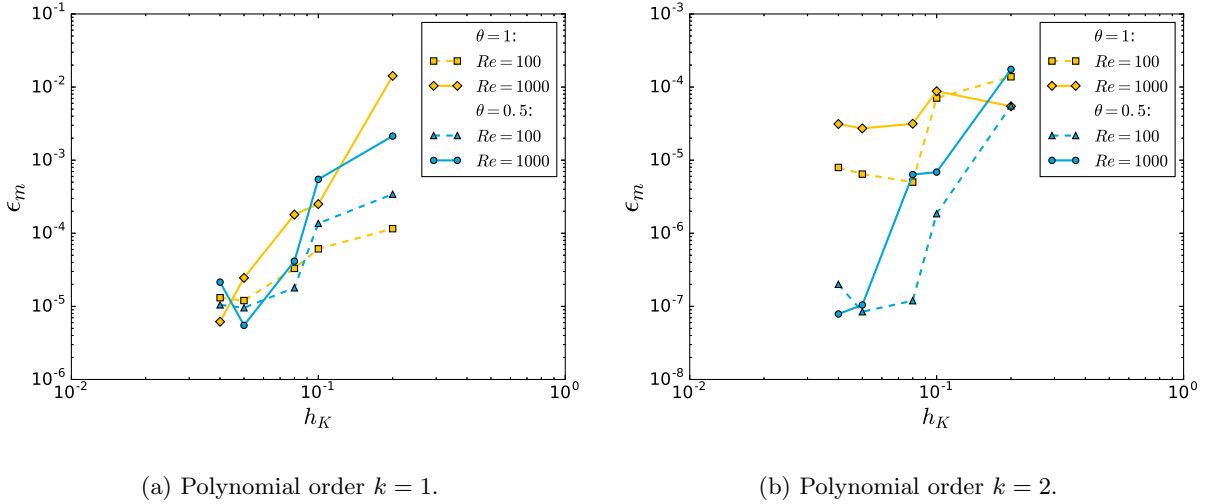


Figure 8: Taylor-Green flow: momentum conservation errors ϵ_m at time $t = 2$ versus the cell size h_K , for $Re = 100$ and $Re = 1000$, and different polynomial orders.

5.3. Benchmark problem: Backward facing step

Flow over a backward facing step is considered for various Reynolds numbers. The problem setup is presented in Fig. 9. The step height H is equal to half the channel diameter D . At the inlet a parabolic
580 velocity profile is prescribed with maximum velocity U_{\max} . Due to the abrupt expansion of the channel, a recirculation zone develops with a Reynolds number dependent reattachment length x_l . The Reynolds number is defined as

$$Re = \frac{\bar{U}D}{\nu}, \quad (60)$$

with $\bar{U} = 2/3 U_{\max}$ denoting the mean inflow velocity and ν the kinematic viscosity.

585 Due to flow separation at the location of the step, a stagnation point in the lower left corner, and the

recirculation and reattachment of the flow past the step, this problem is a demanding test for particle(-mesh) methods.

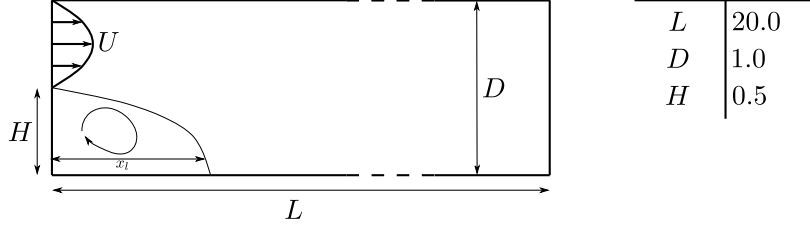


Figure 9: Backward facing step: model setup.

A parabolic inflow velocity with $U_{\max} = 1$ is specified at the inflow boundary of the model domain $\Omega = [0, 20] \times [0, 1]$, that is, for $0.5 \leq y \leq 1$; see Fig. 9. At this boundary, particles are inserted according to the procedure outlined in Section 4. At the outflow boundary at $x = 20$, a homogeneous Neumann boundary condition for the velocity is specified. At the top and the bottom boundary, the no-slip boundary condition $\mathbf{u} = \mathbf{0}$ is specified. The kinematic viscosity ν is adjusted in order to obtain Reynolds numbers ranging from 67 to 800. A regular triangular mesh with $(210 \times 16 \times 2)$ cells is used, and the polynomial orders are $k = m = 2$. The initial particle spacing is set to 0.01, resulting in 30 particles per cell on average. The time step size is set to $\Delta t = 0.04$ resulting in a CFL-number, based on the mean inflow velocity, of approximately 0.4 for all simulations.

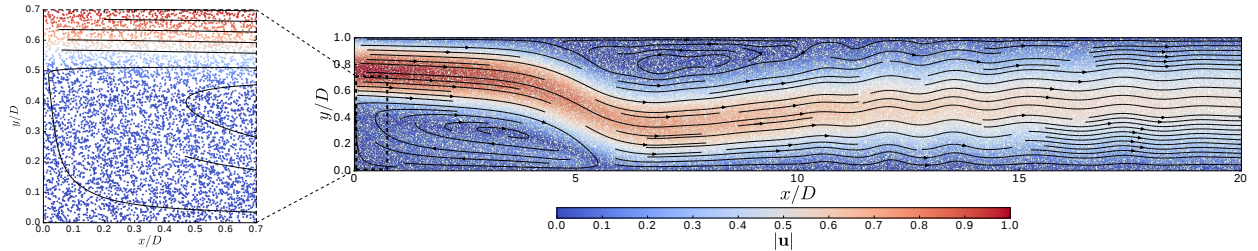


Figure 10: Backward facing step: quasi steady-state particle velocities for $Re = 800$ at $t = 160$, and velocity streamlines obtained from particle velocities (black lines). A detailed view of the particle distribution near the stagnation point is shown in the left panel.

For a Reynolds number of 800, the quasi steady-state solution at time $t = 160$ for the simulated particle velocity field with the corresponding streamlines is plotted in Fig. 10. The computed streamlines involve a recirculation zone in the lower left corner and a secondary recirculation zone near the upper boundary. Of special interest are the particle distributions near the stagnation point in the lower left corner and in the recirculation zones. These zones pose difficulties to, e.g., the SPH method [36], where voids are observed. However, in our method the particle distribution remains uniform over time, even in these critical regions.

In Fig. 11, the computed dimensionless reattachment lengths obtained with the particle-mesh method are compared to values in literature obtained from measurements [37] and numerical experiments [22]. Overall, a very good agreement is found between the computed reattachment lengths and the values found in [22]. This result indicates that the artificial viscosity is low, since the reattachment length is strongly dependent on the Reynolds number. Similarly to the results obtained with the fully Eulerian approach from [22], the model results deviate from the experimental results for $Re > 400$. In various papers [22, 38] this is attributed to the three-dimensional structures present in the experimental setting, which are ignored in the present two-dimensional computations.

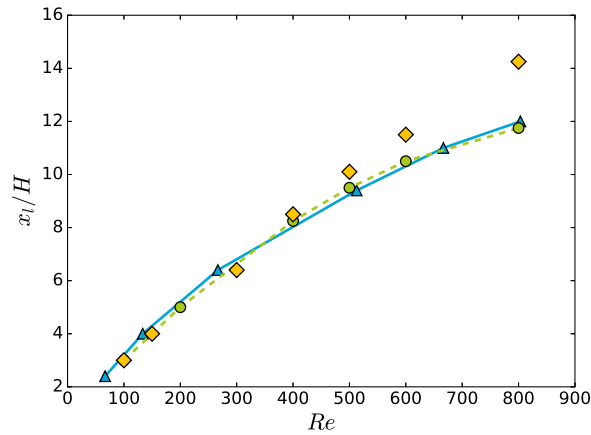


Figure 11: Backward facing step: computed reattachment lengths (Δ) compared with experimental values (\diamond) from Armaly et al. [37], and numerical results (\circ) from Laheur and Wells [22].

5.4. Benchmark problem: Flow past a circular cylinder

As a final benchmark test, the flow around a circular cylinder is considered. Due to the presence of a stagnation point at the upstream part of the cylinder and the occurrence of flow separation at the downstream part of the cylinder, this benchmark is a challenging test when it comes to maintaining a uniform particle distribution.

Apart from assessing the quality of the particle distribution, this benchmark is also used to assess the accuracy of computed dynamic variables such as the drag and lift coefficient and the Strouhal number, the latter indicating the frequency with which vortices are shedded from the cylinder at sufficiently high Reynolds numbers. The setup as presented in the overview paper by Schäfer and Turek [39] is used, see Fig. 12. A boundary-fitted, fully unstructured mesh is used to triangulate the domain of interest.

At the inlet, a parabolic velocity profile is specified as follows,

$$U(0, y) = 4U_{\max}y(H - y)/H^2, \quad (61)$$

and the Reynolds number is defined by Eq. (60), using the mean inlet velocity $\bar{U} = 2/3U_{\max}$.

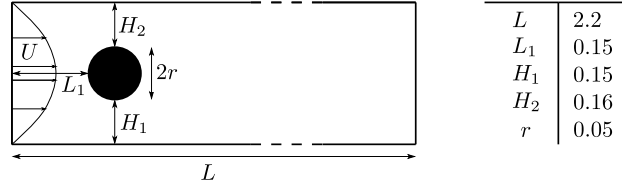


Figure 12: Flow past a circular cylinder: general setup (after [39]).

Following [39], the model is run for Reynolds numbers of 20 and 100 by setting U_{\max} equal to 0.3 and 1.5, respectively, while using a kinematic viscosity $\nu = 10^{-3}$ for both model runs. Quadratic polynomials are used, $k = m = 2$. Furthermore, particles are inserted near the inflow boundaries according to the procedure outlined in Section 4.

Table 3: Flow past a circular cylinder: model settings.

	$Re = 20$	$Re = 100$
U_{\max}	0.3	1.5
$h_{K,\min}$	0.014	0.014
Δt	1e-2	4e-3
$\overline{\Delta p}$	1.75e-3	1.75e-3
CFL (approx.)	0.21	0.43

Other model parameters are listed in Table 3. Note that the CFL-number for the case $Re = 20$ is approximately 0.21, and for the case $Re = 100$ it is approximately 0.43. At the cylinder boundary the no-slip boundary condition is specified, and at the outflow boundary a homogeneous Neumann condition is imposed on the velocity.

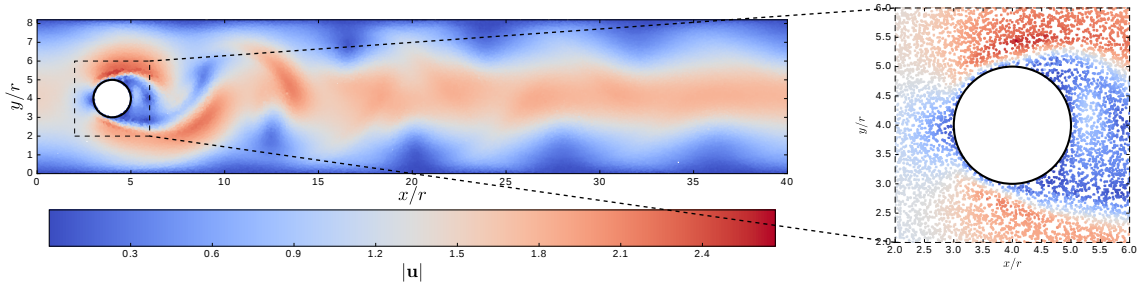


Figure 13: Flow past a circular cylinder: particle velocity field at $t = 8$ for $Re = 100$; a detailed view of the particle distribution near the circular cylinder is shown at the right.

The particle distribution at $t = 8$ for the case $Re = 100$ is shown in Fig. 13. A Reynolds number of 100 is well above the threshold for the onset of vortex shedding, resulting in an unsteady flow characterized by

vortices shedded alternately from the cylinder. This process is also qualitatively observed in Fig. 13.

635 Of special interest is the particle distribution in the vicinity of the cylinder. A detailed view of the area around the cylinder is shown in Fig. 13. The particle distribution remains uniform over time. Moreover, neither unphysical voids nor clusters of particles are observed in the recirculation zone.

Forces exerted on the cylinder for both the low Reynolds number test case and the moderate Reynolds number test case are compared with those reported in [39]. The drag and lift force are expressed in terms
640 of coefficients C_D and C_L , respectively, which are defined as

$$C_D = \frac{F_x}{\rho \bar{U}^2 r}, \quad (62)$$

and

$$C_L = \frac{F_y}{\rho \bar{U}^2 r}, \quad (63)$$

where the force vector $\mathbf{F} = [F_x, F_y]^\top$ acting on the cylinder is computed with

$$645 \quad \mathbf{F} = \int_{\partial\Omega_C} \boldsymbol{\sigma}_h \mathbf{n} d\Gamma, \quad (64)$$

with $\boldsymbol{\sigma}_h$ given by Eq. (32) and $\partial\Omega_C$ denoting the outer boundary of the cylinder.

Following [39] the pressure drop over the cylinder is computed as

$$\Delta P = P(L_1, H_1 + r) - P(L_1 + 2r, H_1 + r). \quad (65)$$

Finally, for the unsteady case ($Re = 100$), the Strouhal number is computed as

$$650 \quad St = \frac{2rf}{\bar{U}}, \quad (66)$$

in which f the frequency with which the flow separation occurs.

Results are tabulated in Table 4 in which also a comparison is made with the reference values from [39]. In general, a good correspondence is observed between the computed quantities and the reference values, the more so as the tabulated differences are well within the range of values presented in [39]. The results for this
655 complex benchmark test demonstrate the accuracy and robustness of the proposed particle-mesh method.

Table 4: Flow past a circular cylinder: model results for different Reynolds numbers, compared to numerical values from Schäfer and Turek [39].

	$Re = 20$				$Re = 100$			
	C_D	C_L	ΔP	St	C_D	C_L	ΔP	St
Simulated	5.74	0.015	0.13	-	3.32	1.27	2.62	0.30
Reference	5.58	0.011	0.1174	-	3.23	1.00	2.48	0.30

6. Conclusions and outlook

The variational framework provided by a hybridized discontinuous Galerkin (HDG) method has been proposed and validated as a particularly attractive and generic approach to formulate particle-mesh methods for the incompressible Navier-Stokes equations. The developed method is cast into an operator splitting approach in which Lagrangian particles are used to discretize an advection operator and an Eulerian HDG approach is employed for the constitutive modeling. The coupling between the Lagrangian particles and the Eulerian mesh is established by means of two auxiliary projection steps. These projections are formulated in terms of an ℓ^2 -minimization problem. Owing to the HDG framework, this strategy results in local projections between the particles and the mesh, which can be implemented efficiently. Moreover, the presented approach allows for a straightforward extension to arbitrary-order spatial accuracy on general meshes. The importance of accurate particle advection was emphasized, advocating the use of second-order accurate time integration methods to update the specific momentum carried by the particles and to update the particle positions by using velocity fields which are almost locally divergence-free. These velocity fields are conveniently obtained when using an HDG method to solve for the unsteady Stokes equations at the background mesh.

The developed scheme was validated for various single-phase problems. Optimal spatial convergence rates were obtained for laminar Poiseuille flow, indicating that the particle-mesh splitting strategy does not affect the spatial accuracy. For the presented time discretization method, second-order accuracy in time was demonstrated.

Maintaining a uniform particle distribution over time was shown to be key to obtain accurate model results. This is achieved by advecting the particles by velocity fields being (nearly) locally divergence-free, and having sufficient inter-element continuity. When these conditions are met, the method is able to accurately resolve the flow near stagnation points, in recirculation zones, and near separation points without the need for additional quality control on the particle distribution. Furthermore, dynamic quantities, such as the reattachment lengths in the backward facing step benchmark and the forces acting on a cylinder, are computed accurately.

The method presented in this paper is promising and deserves further analysis. In this respect, work aiming to eliminate the momentum conservation error is ongoing and the extension to arbitrary order time stepping will be investigated. Moreover, to exploit the full potential of the developed approach, future work will investigate its applicability to multiphase problems and/or problems involving free-surfaces.

Acknowledgements

The Netherlands Organisation for Scientific Research (NWO) is gratefully acknowledged for their support through the JMBC-EM Graduate Programme research grant.

Appendix A. The local ℓ^2 -projections as a specific type of MLS-reconstruction

This appendix shows that on simplices, the proposed (local) ℓ^2 -projections onto the HDG basis can be
 690 considered as a very specific variant of the moving least squares (MLS) reconstruction technique.

Without loss of generality this appendix considers a scalar-valued function $\phi(\mathbf{x})$ that varies in space only, ignoring time dependency. As a result of the latter, the subscripts in the particle set notations are dropped (i.e. \mathcal{S} denotes the time-independent counterpart of \mathcal{S}_t (Eq. (23)) and \mathcal{S}^K denotes the time-independent counterpart of \mathcal{S}_t^K (Eq. (24)).

695 Furthermore, let $\phi_h(\mathbf{x}) \in Q_h$ be an approximation of the scalar-valued function $\phi(\mathbf{x})$ on the piecewise continuous function space Q_h spanned by Lagrange polynomials of order m , see Eq. (19). Let a monomial approximation $\tilde{\phi}_h$ of the scalar-valued function $\phi(\mathbf{x})$ be given by

$$\tilde{\phi}_h(\mathbf{x}) = \mathbf{p}^\top(\mathbf{x}) \mathbf{a}(\mathbf{x}), \quad (\text{A.1})$$

where $\mathbf{a}(\mathbf{x})$ is the (potentially spatially dependent) coefficient vector of the monomial basis $\mathbf{p}^\top(\mathbf{x})$ of order
 700 m . In 1D, this basis has the appearance $\mathbf{p}^\top(x) = [1, x, x^2, \dots, x^m]$.

In MLS, the coefficients $\mathbf{a}(\mathbf{x})$ are obtained by minimizing the residual between the local approximation $\tilde{\phi}_h(\mathbf{x})$ and the scattered particle values, say ϕ_p , in a weighted least-square sense, i.e.

$$\min_{\mathbf{a}(\mathbf{x})} J_1 := \sum_{p \in \mathcal{S}} w(\mathbf{x} - \mathbf{x}_p) (\mathbf{p}^\top(\mathbf{x}_p) \mathbf{a}(\mathbf{x}) - \phi_p)^2, \quad (\text{A.2})$$

with $w(\mathbf{x} - \mathbf{x}_p)$ being a weighting function, usually taken to be symmetric around the particle positions \mathbf{x}_p
 705 and having local support (see e.g. [14, 40]). Furthermore, ϕ_p is a scalar value associated with particle p .

Performing the minimization (see, e.g., [14, 40]) leads to the following expression for the coefficients $\mathbf{a}(\mathbf{x})$:

$$\mathbf{a}(\mathbf{x}) = \mathbf{A}(\mathbf{x})^{-1} \mathbf{B}(\mathbf{x}) \phi_p, \quad (\text{A.3})$$

with

$$\mathbf{A}(\mathbf{x}) = \sum_{p \in \mathcal{S}} \mathbf{p}(\mathbf{x}_p) w(\mathbf{x} - \mathbf{x}_p) \mathbf{p}^\top(\mathbf{x}_p), \quad (\text{A.4})$$

$$\mathbf{B}(\mathbf{x}) \phi_p = \sum_{p \in \mathcal{S}} \mathbf{p}(\mathbf{x}_p) w(\mathbf{x} - \mathbf{x}_p) \phi_p. \quad (\text{A.5})$$

If the particle weighting function $w(\mathbf{x})$ has limited support, the summations in Eq. (A.4) and Eq. (A.5) only involve a (small) subset of the particles in \mathcal{S} . Furthermore, it readily follows that the spatial dependency of the coefficients $\mathbf{a}(\mathbf{x})$ is a result of the weighting function being spatially dependent.

715 To show the similarity between the proposed ℓ^2 -projections and an MLS-reconstruction, consider an ‘indicator’ weighting function, being equal to 1 within the cell K hosting particle p and 0 elsewhere

$$w(\mathbf{x} - \mathbf{x}_p) = \begin{cases} 1, & \text{if } \mathbf{x}_p \in \bar{K}. \\ 0, & \text{otherwise.} \end{cases} \quad (\text{A.6})$$

For this particular choice, Eq. (A.2) results in a sum of independent quadratic forms over all cells $K \in \mathcal{T}$

$$J_1 = \sum_K J_1^K = \sum_K \sum_{p \in \mathcal{S}^K} (\mathbf{p}^\top(\mathbf{x}_p) \mathbf{a} - \phi_p)^2. \quad (\text{A.7})$$

720 The coefficients $\mathbf{a}(\mathbf{x})$ within a cell K are independent of the spatial coordinates $\mathbf{x} \in K$ for this particular choice of the weighting function, see Eq. (A.3).

For the presented ℓ^2 -projections, the minimization problem defined by Eq. (37) for a scalar quantity reads

$$\min_{\phi_h \in Q_h} J_2 := \sum_{p \in \mathcal{S}} (\phi_h(\mathbf{x}_p) - \phi_p)^2. \quad (\text{A.8})$$

This can also be rewritten as a set of independent minimization problems covering all cells $K \in \mathcal{T}$,

$$725 \quad J_2 = \sum_K J_2^K \equiv \sum_K \sum_{p \in \mathcal{S}^K} (\phi_h(\mathbf{x}_p) - \phi_p)^2, \quad (\text{A.9})$$

since $\phi_h \in Q_h$ is discontinuous between cells. Furthermore, $\phi_h(\mathbf{x}_p)$ can be expanded as

$$\phi_h(\mathbf{x}_p) = \sum_i N_i(\mathbf{x}_p) \phi_i \equiv \mathbf{N}(\mathbf{x}_p) \boldsymbol{\phi}, \quad (\text{A.10})$$

in which $N_i(\mathbf{x})$ and ϕ_i denote the discontinuous Lagrange polynomial basis function and (unknown) scalar value at node i , respectively.

730 On simplices, the Lagrange polynomial basis of order m can be rewritten in terms of a monomial basis of order m times a square coefficient matrix \mathbf{C} , i.e.

$$\mathbf{N}(\mathbf{x}) = \mathbf{p}^\top(\mathbf{x}) \mathbf{C}, \quad (\text{A.11})$$

where the coefficient matrix \mathbf{C} is uniquely determined by the element geometry and the Kronecker δ -property. Upon subsequent substitution of Eq. (A.11) in Eq. (A.10) and Eq. (A.9), the latter can be rewritten as

$$735 \quad \sum_K J_2^K = \sum_K \sum_{p \in \mathcal{S}^K} (\mathbf{p}^\top(\mathbf{x}_p) \mathbf{C} \boldsymbol{\phi} - \phi_p)^2. \quad (\text{A.12})$$

Comparing Eq. (A.12) with the minimization problem resulting from an MLS-reconstruction (Eq. (A.7)) readily implies the equality

$$\mathbf{a} \equiv \mathbf{C} \boldsymbol{\phi}, \quad (\text{A.13})$$

where we recall that \mathbf{C} is a square coefficient matrix.

740 Hence, it is concluded that the presented ℓ^2 -projections onto a discontinuous function space can be interpreted as an MLS-reconstruction procedure, using a monomial basis and an element-wise indicator function as particle weighting function, Eq. (A.6). Given this specific choice:

- the coefficients $\mathbf{a}(\mathbf{x}) \equiv \mathbf{a}$ are independent of the spatial coordinates within a cell K . Hence, a (small) matrix has to be inverted once for each cell. From Eq. (A.3) it follows that in general a matrix (albeit being small) has to be inverted for every point at which the MLS-reconstruction is to be evaluated.
- the influence of a particle remains strictly local to the hosting cell.

Appendix B. Time accuracy considerations

This appendix shows that a particle update using Eq. (48) in conjunction with a backward Euler discretization of the Stokes problem (Eq. (47)), results in a scheme being second-order accurate in time.

750 Consider the following representation for the momentum equation in the Stokes problem, using the θ -scheme

$$\frac{\mathbf{u}_h^{n+1} - \mathbf{u}_h^{*,n}}{\Delta t} = \theta \mathbf{F}_h^{n+1} + (1 - \theta) \mathbf{F}_h^n, \quad (\text{B.1})$$

in which \mathbf{F}_h includes all forcing terms (i.e. pressure, viscosity, body forces and boundary terms). Furthermore, $\theta \in [1/2, 1]$ is a parameter, with $\theta = 1$ resulting in a first-order accurate backward Euler scheme and
755 $\theta = 0.5$ yields the second-order accurate Crank-Nicolson method.

We will now show that for the presented particle-mesh splitting, we can obtain second-order overall accuracy in time by combining a backward Euler integration of the Stokes problem with an update of the particle momentum according to Eq. (48).

Since Eq. (B.1) is linear, we can split it as the weighted sum of an implicit and an explicit update, i.e.

$$\frac{\mathbf{u}_h^{n+1} - \mathbf{u}_h^{*,n}}{\Delta t} = \theta \frac{\mathbf{u}_{h,I}^{n+1} - \mathbf{u}_h^{*,n}}{\Delta t} + (1 - \theta) \frac{\mathbf{u}_{h,E}^{n+1} - \mathbf{u}_h^{*,n}}{\Delta t}. \quad (\text{B.2})$$

Combining Eq. (B.2) with Eq. (B.1), the implicit and the explicit part are respectively given by

$$\dot{\mathbf{u}}_{h,I}^{n+1} \equiv \frac{\mathbf{u}_{h,I}^{n+1} - \mathbf{u}_h^{*,n}}{\Delta t} = \mathbf{F}_h^{n+1}, \quad (\text{B.3})$$

$$\dot{\mathbf{u}}_{h,E}^{n+1} \equiv \frac{\mathbf{u}_{h,E}^{n+1} - \mathbf{u}_h^{*,n}}{\Delta t} = \mathbf{F}_h^n. \quad (\text{B.4})$$

765 Comparing the right-hand sides of these equations, it becomes clear that

$$\dot{\mathbf{u}}_{h,E}^{n+1} = \dot{\mathbf{u}}_{h,I}^n. \quad (\text{B.5})$$

Hence, we can write the particle update (Eq. (48)) as

$$\frac{\mathbf{v}_p^{n+1} - \mathbf{v}_p^n}{\Delta t} = \theta \dot{\mathbf{u}}_{h,I}^{n+1}(\mathbf{x}_p^{n+1}) + (1 - \theta) \dot{\mathbf{u}}_{h,E}^{n+1}(\mathbf{x}_p^n), \quad (\text{B.6})$$

$$= \theta \dot{\mathbf{u}}_{h,I}^{n+1}(\mathbf{x}_p^{n+1}) + (1 - \theta) \dot{\mathbf{u}}_{h,I}^n(\mathbf{x}_p^n), \quad (\text{B.7})$$

where the implicit and explicit part have to be evaluated at the new and old position \mathbf{x}_p^{n+1} and \mathbf{x}_p^n , respectively.

From Eq. (B.7) the following observations are made

- Eq. (B.7) is equivalent to the presented mesh-particle projection Eq. (48).
- Hence, second-order accuracy in time can be obtained by storing the implicit result from the previous
775 time step at particle level and reuse it as the explicit part in the current time step.

- The advantage of this ‘particle-based’ second-order accuracy over a ‘mesh-based’ second-order accuracy is that no information needs to be stored at the background mesh between consecutive time steps in the former approach.
- The trade-off of the ‘particle-based’ second-order accuracy is that it requires an initialization step (as $\dot{\mathbf{u}}_{h,I}^n(\mathbf{x}_p^n)$ is not available for $n = 0$) and additional data ($\dot{\mathbf{u}}_{h,I}^n(\mathbf{x}_p^n)$) has to be stored at the particle-level.

References

- [1] M. Evans, F. Harlow, E. Bromberg, The particle-in-cell method for hydrodynamic calculations, Tech. rep., Los Alamos Scientific Laboratory (1957).
- [2] J. Brackbill, H. Ruppel, FLIP: A method for adaptively zoned, particle-in-cell calculations of fluid flows in two dimensions, *J. Comput. Phys.* 65 (2) (1986) 314–343. doi:10.1016/0021-9991(86)90211-1.
- [3] Y. Zhu, R. Bridson, Animating sand as a fluid, *ACM Transactions on Graphics* 24 (3) (2005) 965. doi:10.1145/1073204.1073298.
- [4] D. M. Kelly, Q. Chen, J. Zang, PICIN:a particle-in-cell solver for incompressible free surface flows with two-way fluid-solid coupling, *Journal on Scientific Computing* 37 (3) (2015) 403 – 424. doi:10.1137/140976911.
- [5] Q. Chen, J. Zang, A. S. Dimakopoulos, D. M. Kelly, C. J. Williams, A Cartesian cut cell based two-way strong fluid-solid coupling algorithm for 2D floating bodies, *Journal of Fluids and Structures* 62 (2016) 252–271. doi:10.1016/j.jfluidstructs.2016.01.008.
- [6] J. M. Maljaars, R. J. Labeur, M. Möller, W. S. J. Uijttewaai, A numerical wave tank using a hybrid particle-mesh approach, *Procedia Eng.* 175 (2017) 21–28. doi:10.1016/j.proeng.2017.01.007.
- [7] D. Sulsky, Z. Chen, H. Schreyer, A particle method for history-dependent materials, *Comput. Methods Appl. Mech. Eng.* 118 (1-2) (1994) 179–196. doi:10.1016/0045-7825(94)90112-0.
- [8] S. Kularathna, K. Soga, Implicit formulation of material point method for analysis of incompressible materials, *Comput. Methods Appl. Mech. Eng.* 313 (2017) 673–686. doi:10.1016/j.cma.2016.10.013.
- [9] F. Zhang, X. Zhang, K. Y. Sze, Y. Lian, Y. Liu, Incompressible material point method for free surface flow, *J. Comput. Phys.* 330 (2017) 92–110. doi:10.1016/j.jcp.2016.10.064.
- [10] R. Garg, C. Narayanan, D. Lakehal, S. Subramaniam, Accurate numerical estimation of interphase momentum transfer in Lagrangian-Eulerian simulations of dispersed two-phase flows, *Int. J. Multiph. Flow* 33 (12) (2007) 1337–1364. doi:10.1016/j.ijmultiphaseflow.2007.06.002.
- [11] M. Steffen, R. M. Kirby, M. Berzins, Analysis and reduction of quadrature errors in the material point method (MPM), *Int. J. Numer. Methods Eng.* 76 (6) (2008) 922–948. doi:10.1002/nme.2360.
- [12] Tielen, R and Wobbes, E and Möller, M and Beuth, L, A high order material point method, *Procedia Eng.* 175 (2017) 265–272. doi:10.1016/j.proeng.2017.01.022.
- [13] E. Edwards, R. Bridson, A high-order accurate particle-in-cell method, *Int. J. Numer. Methods Eng.* 90 (9) (2012) 1073–1088. doi:10.1002/nme.3356.
- [14] D. Sulsky, M. Gong, Improving the Material-Point Method, in: *Innovative Numerical Approaches for Multi-Field and Multi-Scale Problems*, Springer International Publishing, 2016, pp. 217–240. doi:10.1007/978-3-319-39022-2_10.
- [15] R. Xu, P. Stansby, D. Laurence, Accuracy and stability in incompressible SPH (ISPH) based on the projection method and a new approach, *J. Comput. Phys.* 228 (18) (2009) 6703–6725. doi:10.1016/j.jcp.2009.05.032.

- [16] R. Vacondio, B. Rogers, P. Stansby, P. Mignosa, J. Feldman, Variable resolution for SPH: A dynamic particle coalescing and splitting scheme, *Comput. Methods Appl. Mech. Eng.* 256 (2013) 132–148. doi:10.1016/j.cma.2012.12.014.
- [17] S. Pope, PDF methods for turbulent reactive flows, *Prog. Energy Combust. Sci.* 11 (2) (1985) 119–192. doi:10.1016/0360-1285(85)90002-4.
- 820 [18] P. Jenny, S. Pope, M. Muradoglu, D. Caughey, A Hybrid Algorithm for the Joint PDF Equation of Turbulent Reactive Flows, *J. Comput. Phys.* 166 (2) (2001) 218–252. doi:10.1006/jcph.2000.6646.
- [19] R. McDermott, S. Pope, The parabolic edge reconstruction method (PERM) for Lagrangian particle advection, *J. Comput. Phys.* 227 (11) (2008) 5447–5491. doi:10.1016/j.jcp.2008.01.045.
- [20] Y. Zhang, D. Haworth, A general mass consistency algorithm for hybrid particle/finite-volume PDF methods, *J. Comput. Phys.* 194 (1) (2004) 156–193. doi:10.1016/j.jcp.2003.08.032.
- 825 [21] R. M. Nestor, M. Basa, M. Lastiwka, N. J. Quinlan, Extension of the finite volume particle method to viscous flow, *J. Comput. Phys.* 228 (5) (2009) 1733–1749. doi:10.1016/j.jcp.2008.11.003.
- [22] R. J. Labeur, G. N. Wells, Energy stable and momentum conserving hybrid finite element method for the incompressible Navier-Stokes equations, *SIAM J. Sci. Comput.* 34 (2) (2012) 889–913. doi:10.1137/100818583.
- 830 [23] A. J. Chorin, Numerical solution of the Navier-Stokes equations, *Math. Comput.* 22 (104) (1968) 745–745. doi:10.1090/S0025-5718-1968-0242392-2.
- [24] R. Témam, Sur l’approximation de la solution des équations de Navier-Stokes par la méthode des pas fractionnaires, *Archive for Rational Mechanics and Analysis* 32 (2) (1969) 135–153. doi:10.1007/BF00247678.
- [25] R. Glowinski, Splitting methods for the numerical solution of the incompressible Navier-Stokes equations., Tech. rep., DTIC Document (1984).
- 835 [26] N. C. Nguyen, J. Peraire, B. Cockburn, A hybridizable discontinuous Galerkin method for Stokes flow, *Comput. Methods Appl. Mech. Eng.* 199 (9-12) (2010) 582–597. doi:10.1016/j.cma.2009.10.007.
- [27] N. Nguyen, J. Peraire, B. Cockburn, An implicit high-order hybridizable discontinuous Galerkin method for the incompressible Navier-Stokes equations, *J. Comput. Phys.* 230 (4) (2011) 1147–1170. doi:10.1016/j.jcp.2010.10.032.
- 840 [28] S. Rhebergen, G. N. Wells, Analysis of a Hybridized/Interface Stabilized Finite Element Method for the Stokes Equations, *SIAM J. Numer. Anal.* 55 (4) (2017) 1982–2003. doi:10.1137/16M1083839.
- [29] D. N. Arnold, F. Brezzi, B. Cockburn, L. D. Marini, Unified Analysis of Discontinuous Galerkin Methods for Elliptic Problems, *SIAM J. Numer. Anal.* 39 (5) (2002) 1749–1779. doi:10.1137/S0036142901384162.
- [30] A. Ralston, Runge-Kutta Methods with minimum error bounds, *Math. Comput.* 16 (80) (1962) 431–437. doi:10.2307/2003133.
- 845 [31] A. Logg, K.-A. Mardal, G. N. Wells, Automated Solution of Differential Equations by the Finite Element Method, Vol. 84, Springer Science & Business Media, 2012. doi:10.1007/978-3-642-23099-8.
- [32] L. D. G. Sigalotti, J. Klapp, E. Sira, Y. Meleán, A. Hasmy, SPH simulations of time-dependent Poiseuille flow at low Reynolds numbers, *J. Comput. Phys.* 191 (2) (2003) 622–638. doi:10.1016/S0021-9991(03)00343-7.
- 850 [33] S. Viswanathan, H. Wang, S. B. Pope, Numerical implementation of mixing and molecular transport in LES/PDF studies of turbulent reacting flows, *J. Comput. Phys.* 230 (17) (2011) 6916–6957. doi:10.1016/j.jcp.2011.05.020.
- [34] S. Subramaniam, D. C. Haworth, A probability density function method for turbulent mixing and combustion on three-dimensional unstructured deforming meshes, *Int. J. Engine Res.* 1 (2) (2000) 171–190. doi:10.1243/1468087001545128.
- [35] P. P. Popov, R. McDermott, S. B. Pope, An accurate time advancement algorithm for particle tracking, *J. Comput. Phys.* 227 (20) (2008) 8792–8806. doi:10.1016/j.jcp.2008.06.021.
- 855 [36] R. Issa, E. S. Lee, D. Violeau, D. R. Laurence, Incompressible separated flows simulations with the smoothed particle hydrodynamics gridless method, *Int. J. Numer. Methods Fluids* 47 (10-11) (2005) 1101–1106. doi:10.1002/flid.864.
- [37] B. F. Armaly, F. Durst, J. C. F. Pereira, B. Schönung, Experimental and theoretical investigation of backward-facing step

flow, *J. Fluid Mech.* 127 (1) (1983) 473–496. doi:10.1017/S0022112083002839.

- 860 [38] J. Kim, P. Moin, Application of a fractional-step method to incompressible Navier-Stokes equations, *J. Comput. Phys.* 59 (2) (1985) 308–323. doi:10.1016/0021-9991(85)90148-2.
- [39] M. Schäfer, S. Turek, F. Durst, E. Krause, R. Rannacher, Benchmark Computations of Laminar Flow Around a Cylinder, in: *Flow Simulation with High-Performance Computers II*, Springer, 1996, pp. 547–566. doi:10.1007/978-3-322-89849-4_39.
- 865 [40] T. Belytschko, Y. Y. Lu, L. Gu, Element-free Galerkin methods, *Int. J. Numer. Methods Eng.* 37 (2) (1994) 229–256. doi:10.1002/nme.1620370205.